The Pennsylvania State University

The Graduate School

College of Engineering

THE EFFECT OF CRYSTALLOGRAPHIC ORIENTATION ON DUCTILE MATERIAL REMOVAL IN SILICON

A Thesis in

Mechanical Engineering

by

Brian P. O'Connor

© 2002 Brian P. O'Connor

Submitted in Partial Fulfillment
of the Requirements
for the Degree of

Master of Science

May 2002

ABSTRACT

In this work, an experimental setup on an ultraprecision machine tool is used to measure the machining forces and critical chip thickness as a function of crystallographic orientation on the (001) face of monocrystalline silicon. The experimental single-point diamond flycutting setup allows shallow (sub micrometer), non-overlapping cuts to be made while minimizing tool track length and sensitivity to workpiece flatness. A high-resolution dynamometer measures machining forces while an acoustic emission sensor mounted to the workpiece chuck detects tool-workpiece contact. The silicon workpiece is inspected using scanning electron microscopy and reflected-light optical microscopy to examine the critical chip thickness as a function of crystallographic orientation.

The test results show that the critical chip thickness and thrust force do vary with crystal orientation. The critical chip thickness is found to be a maximum of 0.4 micrometers along the [100] cutting direction and a minimum of 0.1 micrometers in the [110] cutting direction with a –45º rake tool. The thrust force shows a four-lobed variation that can be correlated with the preferred slip directions in silicon.

This research seeks to advance the state of the art in ductile-regime machining by quantifying the critical chip thickness and machining forces as a function of crystallographic orientation on the cubic face. Once these parameters are known, preferred workpiece orientations can be determined for single-point diamond flycutting.

TABLE OF CONTENTS

LIST OF FIGURES VII

LIST OF TABLES XII

ACKNOWLEDGEMENTS XIII

CHAPTER 1 1
Overview 1
1.1 Introduction 1
1.2 Research Objective 7

CHAPTER 2 8
Properties of Silicon 8
2.1 Atomic Structure and Crystallography of Silicon 8
2.2 Mechanical Properties of Silicon 13
2.2.1 Modulus of Elasticity 13
2.2.2 Shear Modulus 19
2.2.3 Hardness 20
2.2.4 Fracture Toughness 21

CHAPTER 3 23
Literature Review 23
3.1 The Fracture Mechanics Approach 23
3.2 Ductile-regime Machining 29
3.3 Crystallographic Orientation Effects 34

CHAPTER 4 37
Experimental Test Setup 37
4.1 Experimental Test Bed Design 37
4.2 Flycutting Geometry 41
4.3 Machine Metrology 43
4.4 Machine Dynamics 47

CHAPTER 5 52
Experimental Procedure 52
5.1 Machine and Workpiece Preparation 52
5.2 Selection of Machining Variables 54
5.2.1 Diamond Tools 54
5.2.2 Flycutter and Work Spindle Speed 55
5.3 Testing Procedure 56
5.4 Workpiece Metrology 57
5.4.1 Critical Chip Thickness Calculation 57

5.4.2 Sensitivity Analysis 59
5.4.3 Optical Microscopy 61
5.5 Data Post-Processing 62

CHAPTER 6 64
Test Results 64

6.1 -45° Rake Angle Results 64
6.2 0º and –30º Rake Angle Results 69

CHAPTER 7 71
Conclusions and Future Work 71

APPENDIX A 72
Transformation of Stiffness and Compliance Matrices 72

A.1 Rotation around the (001) Crystal Face 74
A.2 Rotation around the (011) Crystal Face 76

APPENDIX B 78
-45º Rake Angle Force Results 78

REFERENCES 80

LIST OF FIGURES

Figure 1.1: Development of achievable machining accuracy over the last century after Taniguchi [1]. Taniguchi developed this metric of machining progression in the early 1980's and shows how he perceived machining evolution up to the year 2000. 2

Figure 1.2: Orthogonal machining illustration of the two material removal regimes; (a) brittle material removal and (b) ductile material removal. In brittle material removal, the undeformed chip thickness is above the material threshold, thus fracture damage is left in the wake of the tool. In ductile material removal, the undeformed chip thickness remains below the critical limit. 5

Figure 2.1: Periodic table of the elements showing an enlarged view of the IV A column. Silicon has an atomic number of 14 and an atomic weight of 28.09. 8

Figure 2.2: Electron configuration for an isolated silicon atom. The 3p energy level can hold up to six total electrons, but for an isolated silicon atom, it holds two. The electrons in the 3s and 3p energy levels are used to form covalent bonds with neighboring atoms. 9

Figure 2.3: Illustration of tetrahedral hybridization where an electron from the 3s orbital moves up into the 3p orbital. The four unpaired electrons can be associated with 4 covalent bonds. 10

Figure 2.4: Tetrahedral configuration of a single silicon molecule. The four covalent bonds are associated with the four unpaired electrons shown in the 3s and 3p energy levels. 10

Figure 2.5: Three-dimensional model of a cubic crystal after [13]. The cubic crystal planes are indicated by (abc) and the crystal directions are indicated by [abc] 11

Figure 2.6: (a) Illustration of the atomic arrangement in a single crystal silicon unit cell (b) as viewed from the [100] direction, (c) as viewed from the [110] direction, and (d) as viewed from the [111] direction. The lattice constant for silicon is 5.43 Å. Notice how the atomic arrangement varies substantially depending on the viewpoint of the crystal lattice. 12

Figure 2.7: Direction surface for Young's modulus of cubic crystal silicon showing the cubic crystal axes. 16

Figure 2.8: Variation of the elastic modulus around the (001) crystal face of silicon. The elastic modulus in the [100] and [110] directions are 130 GPa and 170 GPa, respectively. 17

Figure 2.9: Variation of the elastic modulus around the (011) crystal face of silicon. The elastic modulus in the [110] and [111] directions are 170 GPa and 190 GPa, respectively. The [111] direction is at an angle of 54.74° from the [100] direction. 17

Figure 2.10: Variation of the elastic modulus around the (111) crystal face of silicon. The elastic modulus does not vary as a function of crystallographic direction on this face. The elastic modulus in the [110] and [112] directions is 170 GPa. The [011] and [101] directions are at angles of 60 and 120 degrees, respectively. 18

Figure 2.11: Relative shear occurring between two planes of atoms with atomic spacing, *a*, and an interplanar spacing, *d*. 19

Figure 3.1: Schematic of the crack formation process during point indentation after Lawn and Swain [29]. During the loading cycle (step i-iii), the median crack is formed at some critical load. During unloading (steps iv-vi), the median crack closes and lateral cracks start to form. 24

Figure 3.2: Schematic of crack formation during single-point machining of brittle solids after Swain [30]. (a) crack formation in an orthogonal view and (b) crack formation in a front view. 25

Figure 3.3: Indentation geometry and simplified stress distribution for median crack initiation in an elastic/plastic indentation field after Lawn and Evans [31]. σ_{max} is the max. tensile stress at the elastic/plastic interface, *d* is the depth of penetration below the surface, and *b* is the spatial extent over which the tensile component of the stress field acts. 26

Figure 3.4: Schematic representation of chip formation and machining damage after Blake et. al. [36]. The critical chip thickness is defined as the chip thickness at which subsequent tool passes are unable to remove damage from the previous tool passes 31

Figure 3.5: Schematic of the four different regimes of material response in a plunge-cut made in monocrystalline silicon after Brinksmeier et. al [38] 32

Figure 3.6: Line-force acting on an elastic half-space after Blackley and Scattergood [39] to model crystallographic dependent damage. In polar coordinates, the only nonzero stress component is the radial stress, σ_{rr}, acting a distance r from the point of load application. 34

Figure 3.7: (a) Maximum normalized tensile stress as a function of crystallographic orientation on the (001) crystal face after Blackley and Scattergood [40]. (b) Pitting damage on a machined (001) germanium wafer. 35

Figure 3.8: Variation of maximum normal stress with rake angle for a (001) germanium wafer. 35

Figure 4.1: Experimental setup for silicon flycutting on a Moore Nanotech 150AG. 37

Figure 4.2: Close-up view of the flycutter spindle, workpiece spindle, and instrumentation. 38

Figure 4.3: Close-up view of the PI Twin Mount work spindle with Kistler dynamometer, Kistler acoustic emission sensor, chuck, and silicon workpiece. 39

Figure 4.4: Close-up view of the AC foot/flange flycutter spindle mounted on the x-axis. 40

Figure 4.5: Schematic of the flycutter and workpiece geometry for the silicon flycutting tests. The experimental setup allows for a varying chip thickness over a variety of crystallographic directions in a single test. 41

Figure 4.6: Example of the cuts made on the (001) crystal face of monocrystalline silicon by the silicon flycutting setup. The SEM micrograph is a zoomed view of a few cuts. 42

Figure 4.7: Metrology test setup for measurement of z-axis step performance, z-axis repeatability, and z-axis in-position dither. 43

Figure 4.8: Z-axis step tests for 0.25 micrometer and 1.25 micrometer commanded steps. 44

Figure 4.9: Z-axis unidirectional repeatability tests, 25 mm step away and back towards the capacitance probe. 45

Figure 4.10: Z-axis dither measured with both the z-axis and c-axis servo drives enabled. 46

Figure 4.11: 68-point undeformed experimental modal test grid of the Moore 150AG. 47

Figure 4.12: Drive-point frequency response function. 48

Figure 4.14: The first structural mode of the machine. This mode is the z-axis bouncing on the leadscrew at 128 Hz with 3% damping. This machine mode is the first mode in the sensitive direction during flycutting. 49

Figure 4.15: The second structural mode of the Moore Nanotech150AG. This mode occurs at 290 Hz with 3% damping. This machine mode also occurs in the sensitive direction for the flycutting tests. 50

Figure 4.16: Cross point compliance measurement, $H_{12}(\omega)$ in the sensitive (Z) direction between the flycutter and workpiece chuck. 51

Figure 5.1: Typical 25 mm by 25 mm silicon workpiece made from a polished 150 mm (001) n-type silicon wafer..53

Figure 5.2: The geometry of an individual cut made in a silicon workpiece. The critical dimensions used in the calculation of the critical chip thickness are shown. The length of the overall cut is L_1, the length of the damaged region is L_s, and the depth of cut is *h*...57

Figure 5.3: Simplified cut geometry used to calculate the critical chip thickness. In this figure, *R* is the flycutter radius and t_c represents the critical chip thickness...........58

Figure 5.4: Individual contributions of L_1, L_2, and *R* to the critical chip thickness uncertainty. The uncertainty is calculated for nominal values of the measured variables: L_1 = 1.0 mm, L_2 = 0.9 mm, and *R* = 110 mm...60

Figure 5.5: Nomarski micrograph of multiple cuts in silicon under 20x magnification. These cuts are approximately 20° from the [100] direction. 61

Figure 5.5: Time trace of the filtered and raw thrust force data for a single cut....................62

Figure 5.6: Geometry used to calculate the chip area, *A*..63

Figure 6.1: Measured thrust force time capture over 350º rotation of the workpiece spindle for a –45 degree rake diamond tool. The time capture is not a continuous time representation of the force data. 64

Figure 6.2: Normalized thrust force for a –45º rake tool around the (001) cubic face..........65

Figure 6.3: Schematic of the pitting damage on the (001) crystal face. The white regions correspond to high light scatter caused by severe pitting. In the darker regions, pitting is still present, but much less severe..65

Figure 6.4: Nomarski micrograph of severe pitting damage in the [110] direction under 20x magnification. The depth of cut is 1.2 μm..66

Figure 6.5: Variation in the depth of cut around the cubic crystal face. 67

Figure 6.6: Variation of critical chip thickness with orientation. 0º corresponds to the [100] direction and ± 45º corresponds to the [110] directions..................................67

Figure 6.7: Nomarski micrograph of two cuts under 50x magnification. The top cut is in the [100] direction and the bottom is in the [110] direction......................................68

Figure 6.8: Normalized thrust force data for (a) 0º rake, 1.52 mm nose radius and (b) –30º rake, 1.60 mm nose radius. 69

Figure 6.9: An example of cuts made in silicon with the worn 0º and –30º rake tools. (a) Bright-field microscopy micrograph of multiple cuts made in the [110] direction with a 0º rake tool. (b) An SEM micrograph of the bottom of a cut made with a 0º rake tool in the [110] direction. 70

Figure A.1: Thrust force around cubic crystal face for a nominal depth of cut of 1.0 μm: Test 7, Workpiece 3. 78

Figure A.2: Thrust force around cubic crystal face for a nominal depth of cut of 0.75 μm: Test 8, Workpiece 3. 78

Figure A.3: Thrust force around cubic crystal face for a nominal depth of cut of 0.3 μm: Test 10, Workpiece 4. 79

Figure A.4: Thrust force around cubic crystal face for a nominal depth of cut of 0.4 μm: Test 11, Workpiece 4. 79

LIST OF TABLES

Table 2.1: Stiffness and compliance constants for some selected cubic crystals after [16]. 15

Table 2.2: Knoop indentation hardness of diamond after [23]. 21

Table 2.3: Fracture toughness variation in silicon after Chen and Leipold [24]....22

Table 5.1: Diamond tool properties used in flycutting tests....54

ACKNOWLEDGEMENTS

I would like to sincerely thank my advisor, Dr. Eric Marsh, for giving me the opportunity to work and learn so much from him. He is a great friend and incredibly gifted teacher that has taught me so much over the last few years.

I would like to thank Moore Tool Company, Professional Instruments Company, Aerotech, Edge Technologies, Lion Precision, and Kistler for their gracious supply of equipment and funding. I want to personally thank Dave Arneson of Professional Instruments for teaching me so much about precision machining. The experience I gained working for Dave at Professional Instruments will never be forgotten. I also would like to thank Dave McCloskey, Larry Horner, and Ron Gathagan of the Mechanical Engineering machine shop for allowing me to spend countless hours in the shop with them. In addition, I would like to thank Mark Angelone and John Cantolina of the Materials Characterization Laboratory for help with the workpiece measurement and Professor Paul Cohen for his suggestions and help reviewing this thesis.

I am indebted to all the students of the MDRL for their help and friendship: Jeremiah Couey, Mark Glauner, Bob Grejda, Steve Henry, Byron Knapp, and Dave Schalcosky. They were always willing to help out when help was needed.

I would also like to thank my parents and my brothers for their support and patience throughout my academic career. I would have never made it this far in my academic career without their support and encouragement.

Last, but certainly not least, I would like to thank my fiancée, Heather, for her love and support during some very stressful times. I would have never made it through without her.

CHAPTER 1

OVERVIEW

A brief overview of ultraprecision machining and its application to brittle materials such as silicon is given. The current state of the art in process parameters and machine design in ductile-regime machining is discussed. The motivation for machining brittle materials is also reviewed. In addition, the proposed research approach and motivation for machining silicon is presented.

1.1 INTRODUCTION

Taniguchi defines "ultraprecision machining" as those processes by which the highest possible dimensional accuracy is achieved at a given point in time [1]. Figure 1 shows Taniguchi's view on the development of achievable machining accuracy over the past century. For example, in the 1940s, Moore Special Tool Company's jig grinder design allowed toolmakers to work to levels of accuracy that were previously unachievable [2]. Ultraprecision machining started to become more of a viable manufacturing technique in the 1960's with increased demands in advanced science and technology for energy, computers, electronics, and defense applications [3].

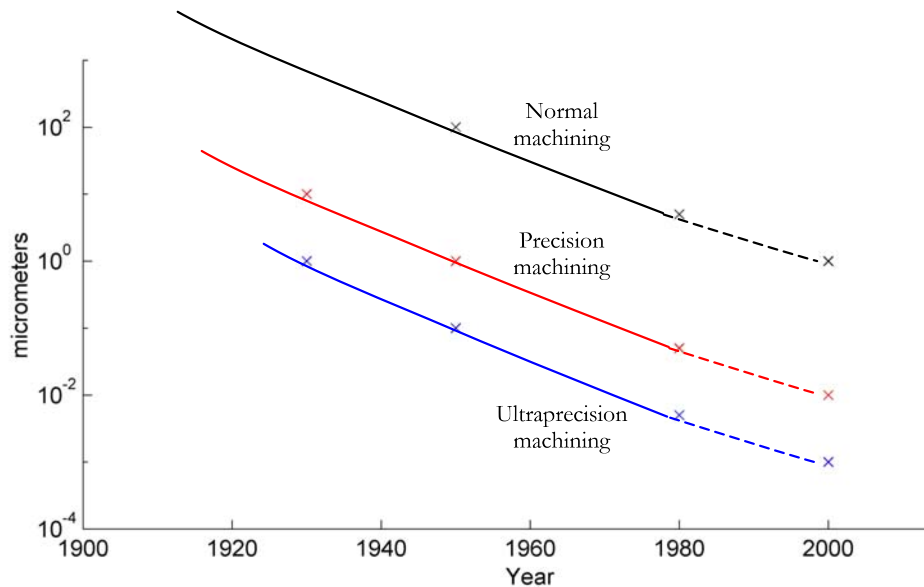

Figure 1.1: Development of achievable machining accuracy over the last century after Taniguchi [1]. Taniguchi developed this metric of machining progression in the early 1980's and shows how he perceived machining evolution up to the year 2000.

Ultraprecision machining includes a variety of grinding, lapping, and turning operations. Modern machine tools used in ultraprecision machining operations require high static and dynamic structural loop stiffness, high-resolution control systems, and low machine error motions.

A specialized subset of ultraprecision machining is diamond turning, where nanometer-level surface finishes and sub micrometer form errors can be obtained using high-accuracy, high-stiffness machines and diamond cutting tools. The use of diamond turning can be traced back to the 1930s when the jewelry industry began diamond turning watch dial components to high surface finishes [4].

Much of the development work in diamond turning was performed during the 1960s and 1970s in government labs such as Lawrence Livermore National Lab (LLNL) and Oak Ridge Y-12 National Lab under Department of Energy and Department of Defense contracts for nuclear weapons and defense research. As the need for large optics in space telescopes and defense systems arose, researchers at LLNL such as Bryan and Donaldson began

designing diamond turning machines with unparalleled size and accuracy. In the late 1970's and early 1980's, Bryan designed a horizontal spindle diamond turning machine that could swing parts slightly over 2 meters (84 inches) in diameter and weighing over 31000 N (7000 lbs) [5]. Donaldson and Patterson designed and constructed a large, vertical axis diamond turning machine with 1.6 meter (64 inch) swing and a 13500 N (3000 lb) load capacity [6]. Despite their size, these machines have accuracies better than 0.1 micrometers using laser interferometer and capacitance probe feedback controls, temperature-controlled environments, and hydrostatic bearings.

Government defense labs such as LLNL and Y-12 gained an interest in generating optics that would require minimal fabrication time and post-polishing using diamond turning techniques. Polishing and lapping of optical flats, spheres, and mirrors may take several weeks, whereas complete fabrication from blanks could be done in substantially less time using diamond turning techniques. In addition, Saito suggests that diamond turning optics may leave the surface and subsurface in a much better metallurgical state compared to polishing and lapping [7].

Early diamond turning work on optics mainly focused on soft materials such as aluminum, copper, electroless nickel, and some polymers. Soft metallic materials such as aluminum and copper are common elements in reflective optics, but often suffer from low specific stiffness, high thermal coefficients of expansion, and oxidation [8]. These materials are inexpensive and easily fabricated; therefore, they are still very common in a variety of optical systems.

As weapons systems became more advanced, the need to machine hard and brittle materials such as glass, ceramics, and crystals became evident. Refractive and diffractive optics used in missile guidance systems and infrared thermal imaging systems required optical

properties that were no longer available with conventional metals such as aluminum. Hard and brittle materials like silicon, germanium, fused silica, quartz, and sapphire became desirable for advanced optics because of their ability to transmit light over a variety of wavelengths [9].

In addition to the needs of the optics community, the semiconductor and opto-electronics industries were looking for more economical ways to manufacture brittle material components such as silicon, germanium, and gallium arsenide. In Japan, sales of high performance semiconductor lasers and other opto-electronics devices reached over $40 billion in 1995 [10]. Even with the wide variety of materials available, more than 90% of all semiconductor products are made out of silicon [11]. With an extremely high-volume industry such as the semiconductor industry, small reductions in manufacturing costs can result in millions of dollars in savings each year.

The trend in manufacturing silicon wafers over the years has been to use numerous grinding, lapping, and polishing steps to produce optical quality, damage-free surfaces. However, silicon has the advantage of being a diamond turnable material based upon its chemical composition [12]. Starting from the Czochralski wafer growth process to final packaging, wafer manufacturing consists of eleven steps [13]. By diamond turning silicon, the number of manufacturing steps could be reduced by minimizing the amount of post-polishing and lapping that is required.

Macroscopically, silicon is a brittle material. Conventional single-point machining in brittle materials such as silicon causes surface and subsurface cracking as a result of damage left by the tool. However, it has been observed that the tendency for subsurface damage to develop lessons with a decrease in the undeformed chip thickness and eventually, disappears at a critical value [14]. Below this material-dependent critical limit, plastic deformation dominates as the main material removal mechanism instead of brittle fracture. This kind of

machining has been termed *ductile-regime machining*. Figure 2 illustrates the difference in the two material removal regimes: brittle and ductile-material removal.

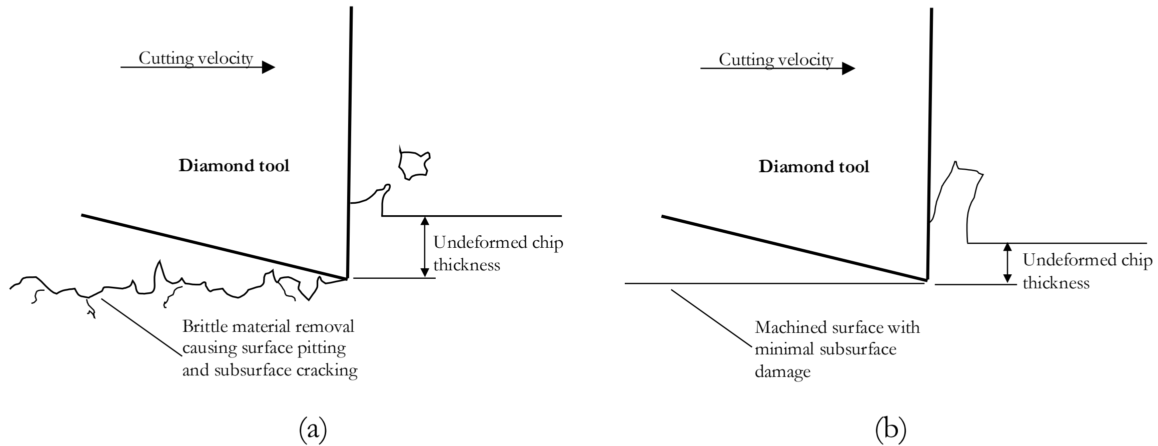

Figure 1.2: Orthogonal machining illustration of the two material removal regimes; (a) brittle material removal and (b) ductile material removal. In brittle material removal, the undeformed chip thickness is above the material threshold, thus fracture damage is left in the wake of the tool. In ductile material removal, the undeformed chip thickness remains below the critical limit.

As previously mentioned, the critical limit (also known as the critical chip thickness or ductile-to-brittle transition depth) varies with the material. In general, most optical and semiconductor materials like silicon have critical chip thicknesses that vary on the order of 0.05 μm – 1 μm [9]. As a result, extremely small depths of cut, low feed rates, and stiff machine tools are required to produce mirror-like surfaces with minimal sub-surface damage. Traditional machine tools are not accurate or stiff enough to machine these materials in the ductile-regime. Therefore, ultraprecision machine tools are required.

Another manufacturing issue that arises when machining single crystals such as silicon is anisotropic material properties. An anisotropic crystal has material properties that vary as a function of crystallographic orientation. This anisotropy also causes machining properties, such as the critical chip thickness, to vary with orientation. Polycrystalline materials usually do

not exhibit large anisotropic properties because each single crystal is randomly oriented in the material thus producing an averaging effect of material properties.

Previous work on the crystallographic-similar diamond indicates that machining along preferred orientations may lower machining forces and mitigate tool wear [15]. If the mechanism for material removal can be better understood along with the knowledge of machining parameters such as cutting forces and critical chip thickness, the anisotropy may be exploited to optimize the machining process.

In a typical facing operation on a lathe, many crystallographic directions of a crystalline material are explored as the workpiece rotates. However, in flycutting and some grinding operations, the kinematics of the process allow for machining in single or a small range of crystallographic directions. It would be extremely advantageous, from a manufacturing standpoint, to machine in the direction with the largest critical chip thickness. A higher critical chip thickness allows heavier cuts and higher feed rates, thus decreasing production time. In addition, knowledge of machining forces is important in reducing tool wear and improving part accuracy. Direction dependent processes such as diamond flycutting may be used to take advantage of crystallographic dependent material properties such as those exhibited by single crystal silicon.

1.2 RESEARCH OBJECTIVE

The objective of this research is to characterize the critical chip thickness and machining forces as a function of crystallographic orientation over the entire (001) silicon crystal face.

Several other researchers have made more traditional attempts to characterize the ductile-to-brittle transition depth by using facing cuts on diamond turning lathes. This approach has a number of disadvantages; namely, damage from previous tool passes does not allow direct measurement of the critical chip thickness. In addition, long tool track lengths lead to significant tool wear resulting in an increase in machining forces. Finally, no information about the effect of crystallographic orientation is gathered.

In this work, an ultraprecision machine tool using two spindles (one workpiece and one flycutter) is used to make interrupted, non-overlapping cuts over the entire crystal face in a single machining setup. Metrology of the workpiece is carried out using microscopy techniques to measure the critical chip thickness. A three-component, milli-Newton resolution force dynamometer is used to measured the machining forces as a function of crystallographic orientation.

The advantage of using the two-spindle flycutter approach is that tool track length is minimized; making tool wear insignificant over the course of a single test. By making non-overlapping cuts, damage from previous tool passes is nonexistent on the machined workpiece. Finally, information about the crystallographic orientation is present in the workpiece as well as the machining force data.

CHAPTER 2

PROPERTIES OF SILICON

Advances in both material science and precision engineering have allowed researchers to better understand the mechanics of ductile-regime material removal. It is therefore necessary to study the material properties of silicon to gain insight into the machining behavior. In this chapter, the crystallography and atomic structure of silicon is discussed. The anisotropy of mechanical properties is presented and the relationship of these properties with silicon machining is examined where appropriate.

2.1 ATOMIC STRUCTURE AND CRYSTALLOGRAPHY OF SILICON

Silicon is the second most abundant element on earth, exceeded only by oxygen [13]. Figure 2.1 shows the location of silicon on the periodic table. It is necessary to understand the properties of silicon on both an atomic viewpoint as well as a macroscopic viewpoint to gain a better understanding of the machining process mechanics.

Figure 2.1: Periodic table of the elements showing an enlarged view of the IV A column. Silicon has an atomic number of 14 and an atomic weight of 28.09.

An isolated silicon atom has 14 electrons. The electron energy level configuration for silicon is $1s^2 2s^2 2p^6 3s^2 3p^2$. The electron configuration for a single silicon atom is shown Figure 2.2. The lightly shaded spots in the 3p orbital indicate the number of vacant electrons (electrons needed to fill orbital).

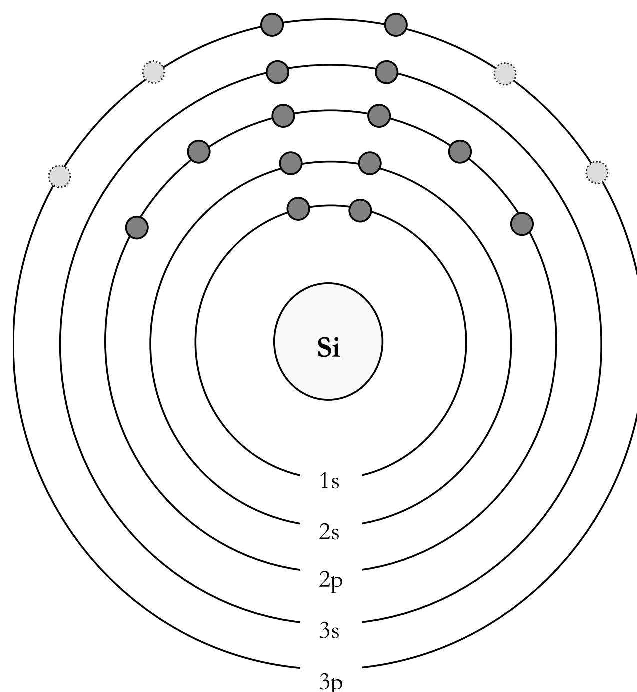

Figure 2.2: Electron configuration for an isolated silicon atom. The 3p energy level can hold up to six total electrons, but for an isolated silicon atom, it holds two. The electrons in the 3s and 3p energy levels are used to form covalent bonds with neighboring atoms.

The electrons in the 3s and 3p energy levels contribute to forming the covalent bond with neighboring silicon atoms. To complete covalent bonding, one of the 3s electrons is transferred to the 3p orbital resulting in an sp^3 orbital hybridization known as *tetrahedral hybridization* [13]. An illustration of this transferal of electrons is shown in Figure 2.3.

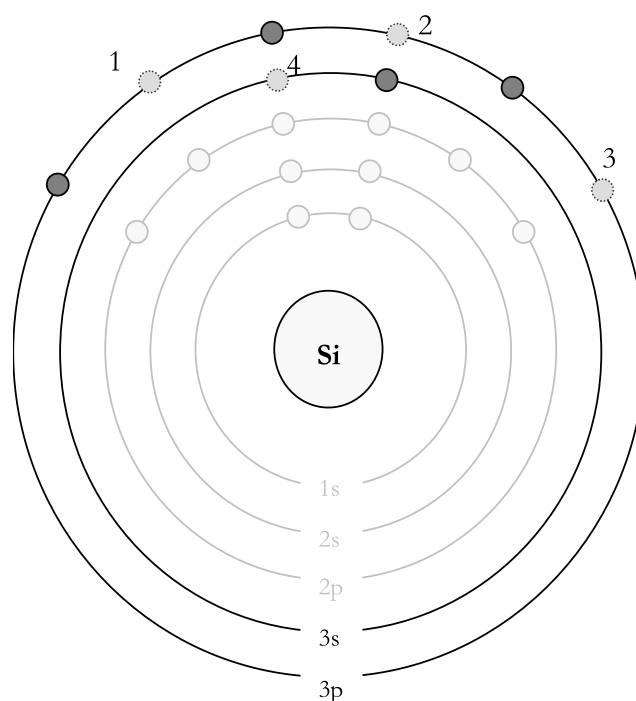

Figure 2.3: Illustration of tetrahedral hybridization where an electron from the 3s orbital moves up into the 3p orbital. The four unpaired electrons can be associated with 4 covalent bonds.

The 1s, 2s, and 2p energy levels do not contribute to the forming of the covalent bond. The four unpaired electrons form four covalent bonds in a tetrahedral configuration. The tetrahedral bonding configuration of a silicon molecule is shown in Figure 2.4.

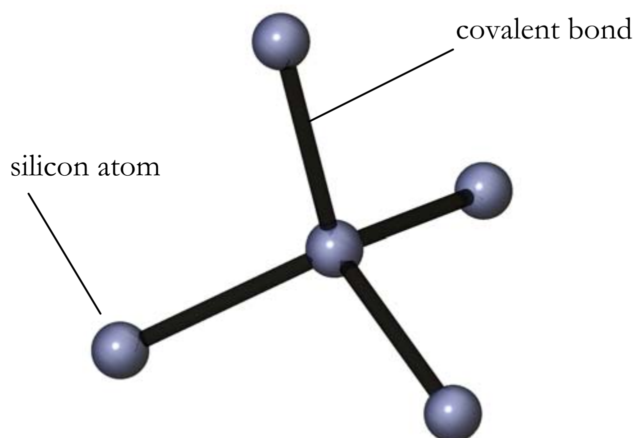

Figure 2.4: Tetrahedral configuration of a single silicon molecule. The four covalent bonds are associated with the four unpaired electrons shown in the 3s and 3p energy levels.

Single crystal silicon is a cubic crystal with a diamond (tetrahedral) structure. The planes of silicon can be described using Miller indices. The easiest way to visualize the positions of the crystal planes in silicon is by a three-dimensional model shown in Figure 2.5 after Shimura [13].

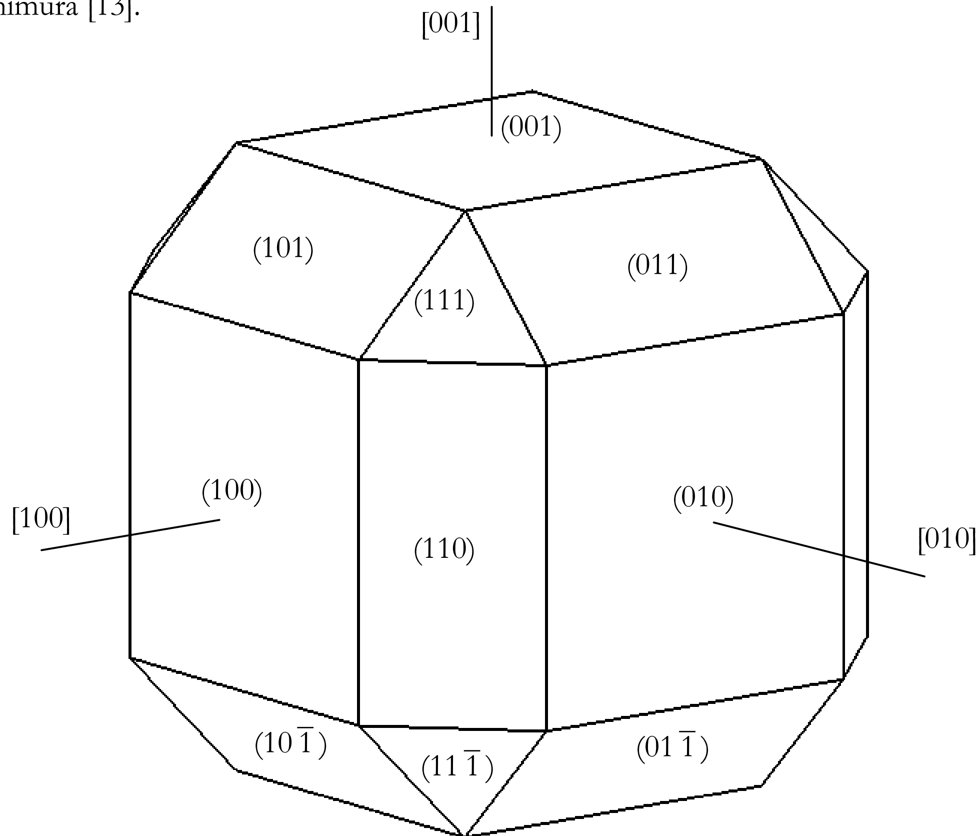

Figure 2.5: Three-dimensional model of a cubic crystal after [13]. The cubic crystal planes are indicated by (abc) and the crystal directions are indicated by [abc].

A model of the silicon crystal lattice is shown in Figure 2.6. Three different views of the silicon lattice are also shown. The structure of the silicon crystal lattice and atomic arrangement are extremely important in determining the anisotropy of silicon. This characteristic atomic arrangement affects the mechanical, electrical, and optical properties of silicon. The mechanical anisotropy is especially influential in the crystallographic effects found in machining silicon.

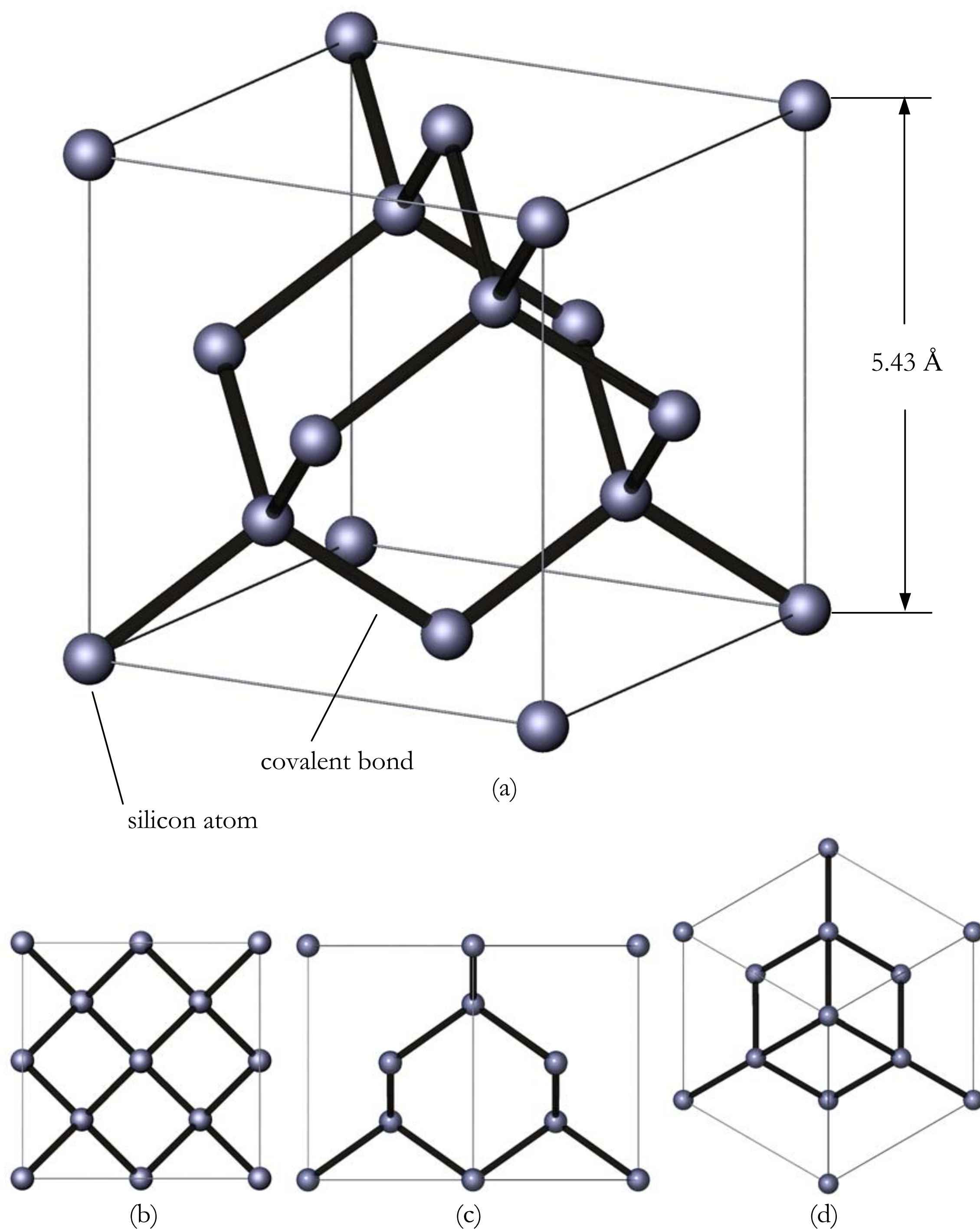

Figure 2.6: (a) Illustration of the atomic arrangement in a single crystal silicon unit cell (b) as viewed from the [100] direction, (c) as viewed from the [110] direction, and (d) as viewed from the [111] direction. The lattice constant for silicon is 5.43 Å. Notice how the atomic arrangement varies substantially depending on the viewpoint of the crystal lattice.

2.2 MECHANICAL PROPERTIES OF SILICON

As mentioned in the previous section, the arrangement of atoms in the crystal lattice plays a very important role in the anisotropy of mechanical properties. Some of the mechanical properties that are believed to be influential in determining the machining behavior of silicon are discussed.

2.2.1 MODULUS OF ELASTICITY

In general, Hooke's law states that in an elastic material for sufficiently small deformations, the stress is directly proportional to the strain. Hooke's law is expressed in tensor form as

$$\sigma_{ij} = c_{ijkl}\varepsilon_{kl} \tag{2.1}$$

where σ_{ij} is the stress tensor, ε_{kl} is the strain tensor, and c_{ijkl} is the fourth-order elastic stiffness tensor. Similarly, the strains are proportional to the stresses by

$$\varepsilon_{ij} = s_{ijkl}\sigma_{kl} \tag{2.2}$$

where s_{ijkl} is a fourth-order tensor known as the elastic compliance tensor. Equation (2.1) can also be represented in matrix form as

$$\begin{bmatrix} \sigma_x \\ \sigma_y \\ \sigma_z \\ \tau_{xy} \\ \tau_{yz} \\ \tau_{zx} \end{bmatrix} = \begin{bmatrix} c_{11} & c_{12} & c_{13} & c_{14} & c_{15} & c_{16} \\ c_{21} & c_{22} & c_{23} & c_{24} & c_{25} & c_{26} \\ c_{31} & c_{32} & c_{33} & c_{34} & c_{35} & c_{36} \\ c_{41} & c_{42} & c_{43} & c_{44} & c_{45} & c_{46} \\ c_{51} & c_{52} & c_{53} & c_{54} & c_{55} & c_{56} \\ c_{61} & c_{62} & c_{63} & c_{64} & c_{65} & c_{66} \end{bmatrix} \begin{bmatrix} \varepsilon_x \\ \varepsilon_y \\ \varepsilon_z \\ \gamma_{xy} \\ \gamma_{yz} \\ \gamma_{zx} \end{bmatrix} \tag{2.3}$$

As a result, there are 36 independent elastic constants. It can be shown by a thermodynamic argument that this number can be reduced to 21, thus making the stiffness

matrix, [c], symmetric [16]. For a cubic crystal such as monocrystalline silicon, the number of independent constants can be further reduced to three (c_{11}, c_{12}, and c_{44}) [17].

Therefore, for a cubic crystal, equation (2.3) can be rewritten as

$$\begin{bmatrix} \sigma_x \\ \sigma_y \\ \sigma_z \\ \tau_{xy} \\ \tau_{yz} \\ \tau_{zx} \end{bmatrix} = \begin{bmatrix} c_{11} & c_{12} & c_{12} & 0 & 0 & 0 \\ c_{12} & c_{11} & c_{12} & 0 & 0 & 0 \\ c_{12} & c_{12} & c_{11} & 0 & 0 & 0 \\ 0 & 0 & 0 & c_{44} & 0 & 0 \\ 0 & 0 & 0 & 0 & c_{44} & 0 \\ 0 & 0 & 0 & 0 & 0 & c_{44} \end{bmatrix} \begin{bmatrix} \varepsilon_x \\ \varepsilon_y \\ \varepsilon_z \\ \gamma_{xy} \\ \gamma_{yz} \\ \gamma_{zx} \end{bmatrix} \tag{2.4}$$

The elastic compliance matrix, [s], is the inverse of the elastic stiffness matrix, [c]. Therefore, the compliance matrix can be written as

$$[s] = [c]^{-1} = \begin{bmatrix} s_{11} & s_{12} & s_{12} & 0 & 0 & 0 \\ s_{12} & s_{11} & s_{12} & 0 & 0 & 0 \\ s_{12} & s_{12} & s_{11} & 0 & 0 & 0 \\ 0 & 0 & 0 & s_{44} & 0 & 0 \\ 0 & 0 & 0 & 0 & s_{44} & 0 \\ 0 & 0 & 0 & 0 & 0 & s_{44} \end{bmatrix} \tag{2.5}$$

where the resultant compliance terms, s_{ij}, are related to the stiffness terms, c_{ij}, by the following relations

$$s_{11} = \frac{(c_{11} + c_{12})}{(c_{11} - c_{12})(c_{11} + 2c_{12})} \tag{2.6}$$

$$s_{12} = -\frac{c_{12}}{(c_{11} - c_{12})(c_{11} + 2c_{12})} \tag{2.7}$$

$$s_{44} = \frac{1}{c_{44}} \tag{2.8}$$

The values for the stiffness constants (c_{11}, c_{12}, and c_{44}) and compliance constants (s_{11}, s_{12}, and s_{44}) for silicon as well as some other cubic crystals are shown in Table 2.1.

Table 2.1: Stiffness and compliance constants for some selected cubic crystals after [16].

Material	Stiffness (GPa)			Compliance (10^{-12} Pa^{-1})		
	c_{11}	c_{12}	c_{44}	s_{11}	s_{12}	s_{44}
Diamond	1020	250	492	1.12	-0.22	2.07
Silicon	165.7	63.9	79.56	7.68	-2.14	12.56
Germanium	128.9	48.3	67.1	9.78	-2.66	14.9
Gallium Arsenide	118.8	53.8	59.4	12.64	-4.23	18.6
Lithium Fluoride	111.2	42.0	62.8	11.35	-3.1	15.9
Sodium Fluoride	97	24.4	28.1	11.5	-2.3	35.6
Alum., single crystal	108	61.3	28.5	15.9	-5.8	35.2
Silver, single crystal	119	89.4	43.7	23.2	-9.93	22.9
Gold, single crystal	186	157	42	23.3	-10.7	23.8

The elastic modulus, as defined by Nye, is the ratio of the longitudinal stress to the longitudinal strain [18] and is commonly referred to in literature as

$$E_i = \frac{1}{s_{ii}} \tag{2.8}$$

where i = 1, 2, or 3. In order to visualize the anisotropy of the elastic modulus, a three-dimensional surface can be created called the *direction surface of Young's modulus* [19]. This surface is constructed using rotation transformations of the compliance constants about general crystal axes. The mathematical background for the general formulation is given in [16,18,19]. Nye gives the equation for the inverse of Young's modulus for a cubic crystal in the direction of the unit vector, l_i, as

$$E^{-1} = s_{11} - 2\left(s_{11} - s_{12} - \frac{1}{2}s_{44}\right)\left(l_1^2 l_2^2 + l_2^2 l_3^2 + l_1^2 l_3^2\right) \tag{2.9}$$

This can be written in spherical coordinates as

$$E^{-1} = s_{11} - 2\left(s_{11} - s_{12} - \frac{1}{2}s_{44}\right)\left[sin^2\theta\left(cos^2\theta + sin^2\theta\, sin^2\psi\, cos^2\psi\right)\right] \tag{2.10}$$

where θ and ψ are the polar and azimuth angles, respectively, relative to the cubic axes. Figure 2.7 shows the direction surface for the elastic modulus of silicon.

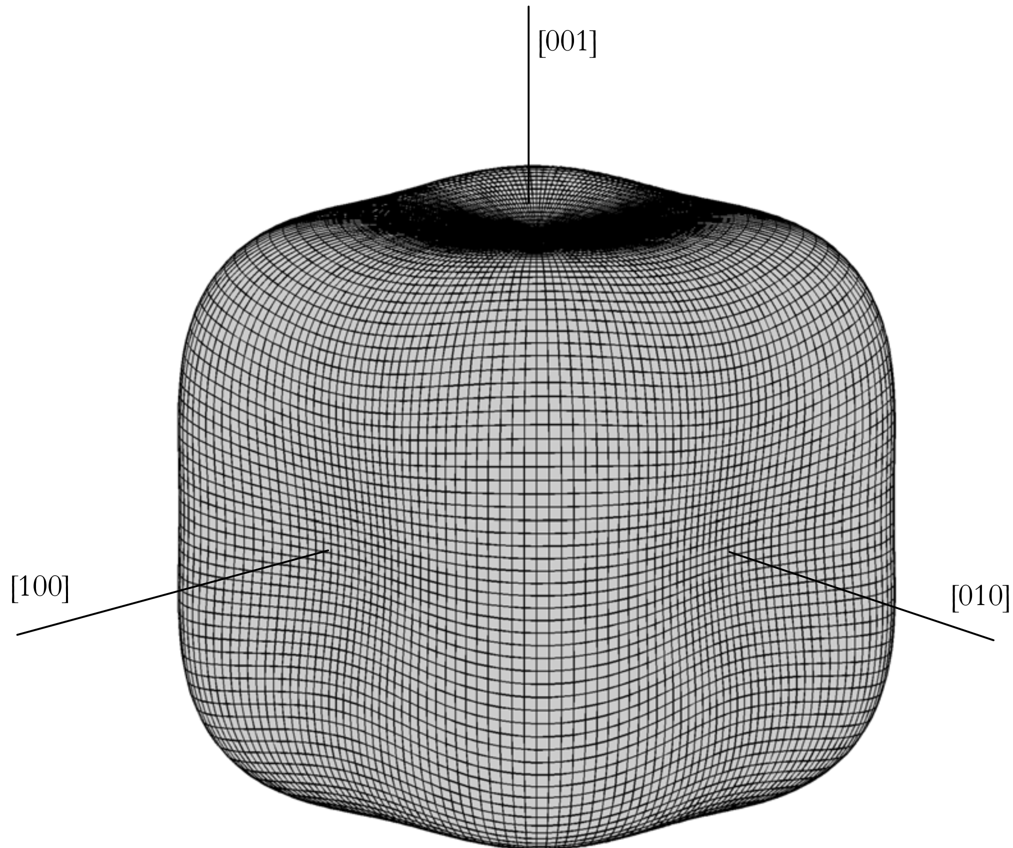

Figure 2.7: Direction surface for Young's modulus of cubic crystal silicon showing the cubic crystal axes.

The variation of the elastic modulus on individual crystal planes is found by taking "slices" of the three-dimensional direction surface through the origin of the crystal axes. The Bond method is useful for obtaining the variation of Young's modulus for a given crystal plane [16]. The Bond method, outlined in Appendix A, uses 6x6 rotation transformation matrices to transform the stiffness and compliance matrices in different crystallographic directions. Figure 2.8, 2.9, and 2.10 represent the variation of the elastic modulus on the (001), (011), and (111) crystal planes, respectively.

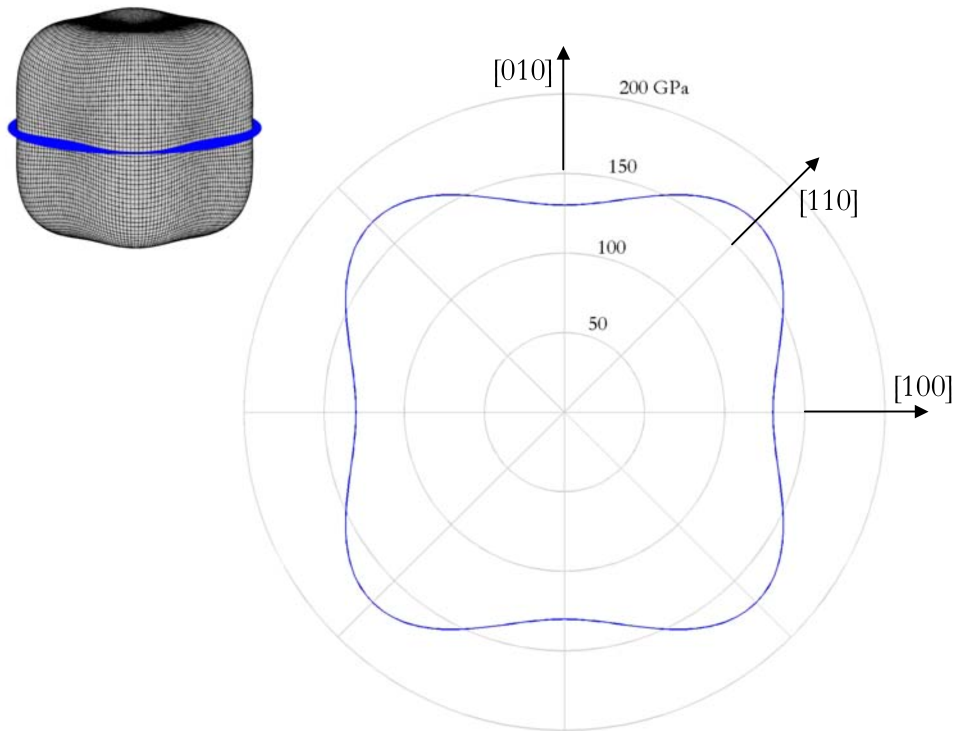

Figure 2.8: Variation of the elastic modulus around the (001) crystal face of silicon. The elastic modulus in the [100] and [110] directions are 130 GPa and 170 GPa, respectively.

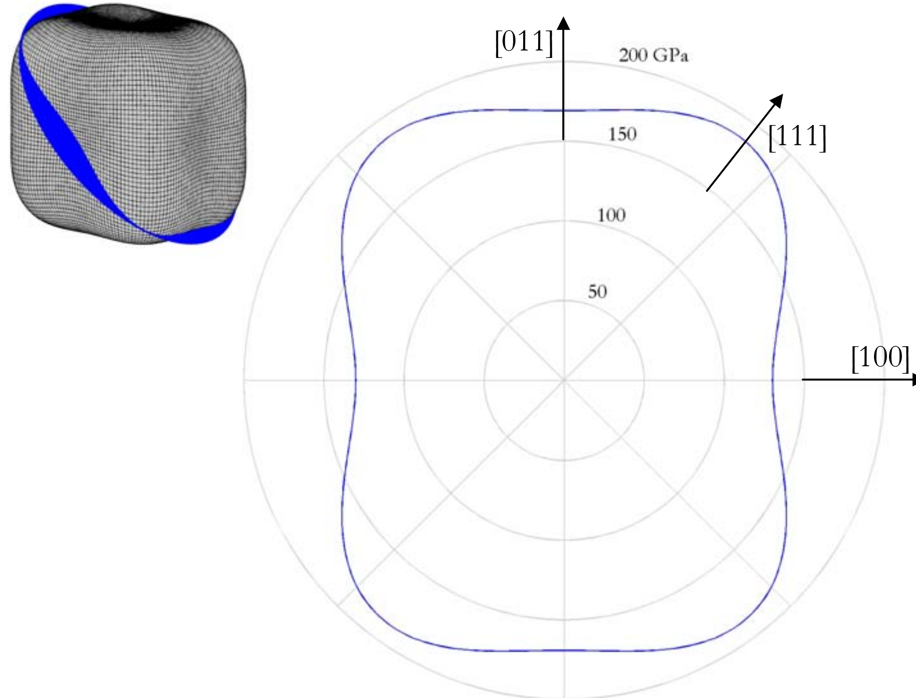

Figure 2.9: Variation of the elastic modulus around the (011) crystal face of silicon. The elastic modulus in the [110] and [111] directions are 170 GPa and 190 GPa, respectively. The [111] direction is at an angle of 54.74° from the [100] direction.

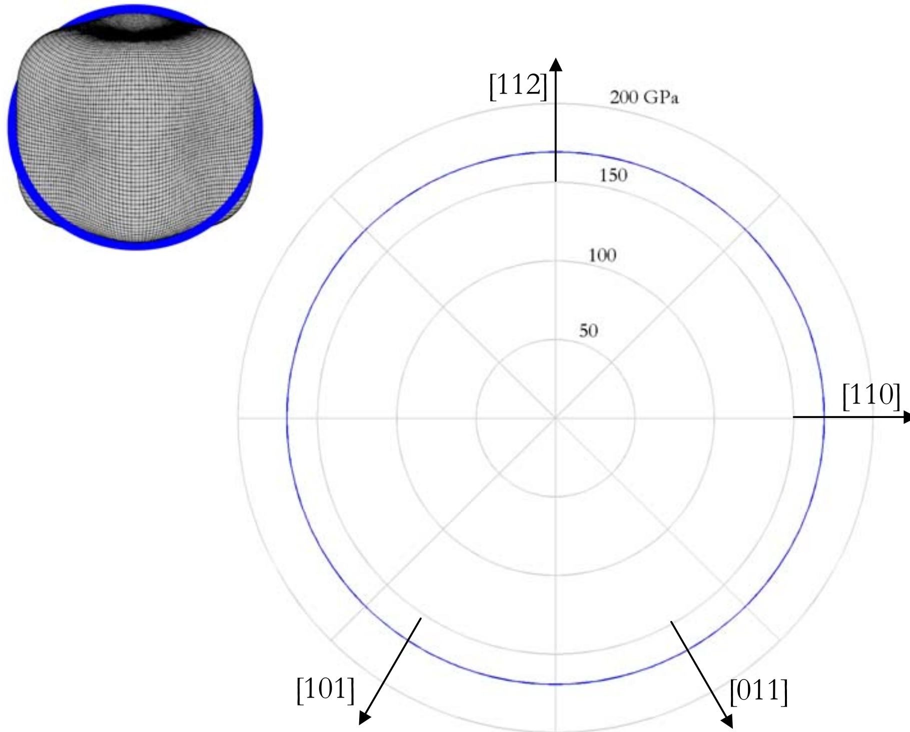

Figure 2.10: Variation of the elastic modulus around the (111) crystal face of silicon. The elastic modulus does not vary as a function of crystallographic direction on this face. The elastic modulus in the [110] and [112] directions is 170 GPa. The [011] and [101] directions are at angles of 60 and 120 degrees, respectively.

The variation of the elastic modulus in silicon is very important for manufacturing processes. Researchers at the Commonwealth Scientific and Industrial Research Organization (CSIRO) in Australia are using single crystal silicon spheres for the accurate determination of Avogadro's number [20]. Collins, et. al. have found that the sphericity obtained by the grinding and polishing of these spheres can be explained in terms of the variation of Young's modulus with crystallographic direction [20]. The shape of the machined silicon sphere matched the cubic shape of the direction surface of Young's modulus. They explained the results in terms of the cleavage energy, γ (the work per unit area needed to pull the atoms apart). The energy needed to create two new surfaces is then given as

$$2\gamma \approx \frac{2Ea}{\pi^2} \tag{2.11}$$

where a is the atomic spacing and E is the elastic modulus. Their conclusion was that if the grinding and polishing does uniform work per unit area, then the amount of material removed in any one direction will vary as the inverse of the elastic modulus due to equation (2.11).

2.2.2 SHEAR MODULUS

The shear modulus plays an important role in governing plastic properties such as slip deformation and yielding in crystals. In ductile-regime machining, plastic deformation dominates over fracture as the main material removal mechanism. In general, there are three shear modulii for an anisotropic crystal. For a cubic crystal, they are given as

$$G_{12} = \frac{1}{s_{66}} \tag{2.12}$$

$$G_{13} = \frac{1}{s_{55}} \tag{2.13}$$

$$G_{23} = \frac{1}{s_{44}} \tag{2.14}$$

Figure 2.11 shows two adjacent planes of atoms separated by distance, d, and with an atomic spacing, a, where relative shear exists. This is an illustration of the relative movement between planes of atoms in the plastic deformation process that occurs in ductile-regime machining.

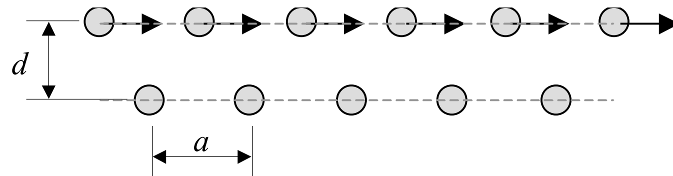

Figure 2.11: Relative shear occurring between two planes of atoms with atomic spacing, a, and an interplanar spacing, d.

The maximum, or critical, shear stress in which the lattice becomes unstable and irrereversible plastic deformation occurs is given by Kittel [17] as

$$\tau_c = \frac{G_{ij} a}{2\pi d} \tag{2.13}$$

where G_{ij} is the shear modulus in the direction of the slip motion, a is the atomic spacing, and d is the spacing between the planes of slip. It is easily seen that the critical shear stress varies as a function of crystallographic orientation due to the crystallographic dependence of the shear modulus, G_{ij}. The shear modulus can easily be calculated using the same methods used to calculate the elastic modulus as a function of crystallographic orientation.

2.2.3 HARDNESS

Hardness is defined as a measure of a materials resistance to deformation by surface indentation or abrasion [21]. In general, the harder the material, the more difficult the material is to machine. The nature of hardness anisotropy is governed by the crystal structure of the material and the primary slip systems that aid dislocation motion during indentation [22]. It has been found that the crystallographic directions that correspond to minimum values of the effective resolved shear stress are found to be those of maximum hardness [23]. Brookes and Burnand [23] give the effective resolved shear stress as

$$\tau_e = \frac{F}{2A}(cos\,\psi + sin\,\gamma)cos\,\alpha\, cos\,\lambda \tag{2.14}$$

where F is the applied load, A is the projected area supporting the load, ψ is the angle between each face of the indenter and the axis of rotation for the slip system, γ is the angle between each face of the indenter and the slip direction, α is the angle between the axis of the applied

load and the normal vector to the slip plane, and λ is the angle between the axis of the applied load and the slip direction.

The primary slip system in silicon is on the highest atomic density {111} planes in the closest-packed [110] direction. The effective resolved shear stress is a good qualitative tool to describe the hardness anisotropy in crystals. Therefore, hardness measurements using either a Knoop or Vickers indenter are needed to quantify the hardness in different crystallographic directions. Knoop hardness values for single crystal diamond are shown in Table 2.2.

Table 2.2: Knoop indentation hardness of diamond after [23].

Crystal Plane	Direction	Hardness (kg/mm^2)
(001)	[110]	6900
(001)	[100]	9600
(011)	[110]	7400
(011)	[111]	6200
(111)	[112]	9000

One would expect to see the same percentage variations of hardness in silicon as in diamond because they both have the same crystallographic structure. Diamond exhibits a 28% variation of hardness between the [110] direction and [100] direction on the (001) crystal face. Similarly, a 16% variation in hardness is found between the [111] direction and [110] direction on the (011) crystal face.

2.2.4 FRACTURE TOUGHNESS

Fracture toughness is also important in understanding the machining process of silicon. As previously mentioned, in ductile-regime machining, plasticity is the dominant material removal mechanism. Fracture mechanics, however, may help in understanding how the transition is made from ductile material removal to brittle fracture. One of the most important parameters in fracture mechanics is fracture toughness. Fracture toughness is defined as the critical value

of the stress intensity factor for which crack extension occurs [21]. The fracture toughness, K_c, is related to the crack dimensions and the material-dependent critical stress by the equation,

$$K_c = \psi \sigma_c \sqrt{\pi a} \tag{2.15}$$

where ψ is a dimensionless constant that depends on the crack geometry and the type of loading, σ_c is the critical stress for crack propagation, and a is the characteristic crack length [21].

For silicon, the fracture toughness is found to vary with the crystal plane orientation. Chen and Leipold give the values of fracture toughness in certain crystal planes [24]. Table 2.3 gives values for fracture toughness at room temperature for three crystal planes in silicon.

Table 2.3: Fracture toughness variation in silicon after Chen and Leipold [24].

Crystal plane	Fracture toughness (MPa√m)
(100)	0.95
(110)	0.90
(111)	0.82

Although no information is given about the crystallographic orientation of the fracture toughness measurement on each plane, these values are a good indication of the amount of variation in single crystal silicon.

CHAPTER 3

LITERATURE REVIEW

The literature covered in this review focuses on work done by other researchers to understand the mechanics of ductile-regime machining through experiments and analysis. It is generally understood that fracture mechanics may yield an explanation into the physics involved in brittle material machining; therefore, an attempt is made to include relevant indentation and fracture mechanics models into the review. However, an in-depth treatment of the mathematical theory is not given; thus the reader is referred to the references for a more thorough treatment. In addition, models by other researchers attempting to describe the effect of crystallographic orientation on ductile-regime machining are discussed.

3.1 THE FRACTURE MECHANICS APPROACH

The mechanisms involved in causing a brittle material to deform plastically are highly debated. However, there is little dispute that a "size effect" exists in ductile-regime machining; that is, as critical dimensions (such as undeformed chip thickness and machining forces) get smaller, material is removed by plastic deformation instead of fracturing. A large effort in explaining ductile-regime machining has focused on the science of indentation and fracture mechanics.

Fracture mechanics approaches to modeling the machining process of brittle materials focus on how cracks initiate and are propagated into the material. Crack initiation in deformation processes tends to nucleate at points of intense stress concentration ahead of the zones of inelastically deformed material [25]. Fracture occurs as the critical size (flaw size, indentation depth, machining depth, etc.) becomes larger. However, as the undeformed

volume of material becomes small enough, plastic deformation becomes more energetically favorable over crack initiation and propagation [26].

In machining operations such as turning and grinding, two principal crack systems have the capability of forming as the cutting tool is traversed across the workpiece: the median crack and the lateral crack [27, 28]. In general, median crack formation is generally associated with strength degradation of the material, while lateral crack formation is generally associated with material removal processes [28]. Lawn and Swain [29] noticed that a general pattern of crack formation and propagation emerged from quasi-static indentation studies in brittle materials. This crack formation process is shown in Figure 3.1.

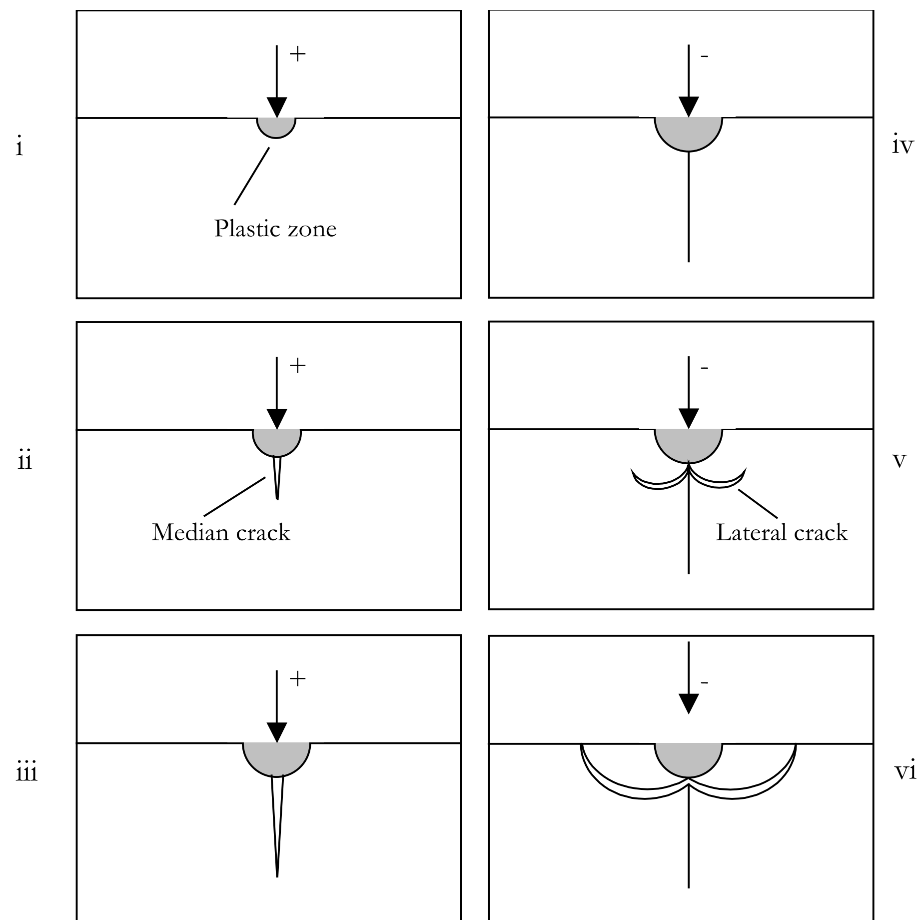

Figure 3.1: Schematic of the crack formation process during point indentation after Lawn and Swain [29]. During the loading cycle (step i-iii), the median crack is formed at some critical load. During unloading (steps iv-vi), the median crack closes and lateral cracks start to form.

When the load and indentation size are below a critical limit, plastic deformation occurs (step i). When the load is increased beyond a critical value, a median crack starts to form at the edge of the plastic zone and continues to propagate into material (steps ii and iii). As the compressive load is decreased, the median crack starts to close (step iv). Relaxation of the deformed material within the plastic zone superimposes large residual tensile stresses upon the applied stress field and causes lateral crack formation (step v). As the load is completely removed (step vi), the lateral crack system extends until equilibrium is achieved.

For indentation, the crack system is largely two-dimensional as seen in Figure 3.1. For diamond turning and scratching, the crack system also propagates in the wake of the tool. Swain [30] noticed that when scratching brittle solids with an indenter, the median and lateral crack systems propagated as shown in Figure 3.2.

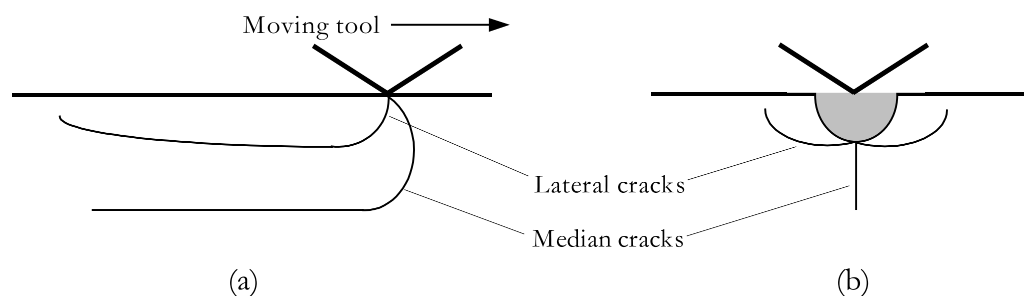

Figure 3.2: Schematic of crack formation during single-point machining of brittle solids after Swain [30]. (a) crack formation in an orthogonal view and (b) crack formation in a front view.

Depending upon the severity of the residual tensile stress field, the subsurface lateral cracks may propagate up to the surface of the material leaving pitting damage on the machined workpiece. If the cracks do not propagate to the surface, subsurface damage is still present. The surface and subsurface damage left from the machining process have adverse effects on the final part value. Therefore, it is desirable to stay below the material and geometrical-dependent critical size and load in order to prevent crack initiation.

In 1977, Lawn and Evans [31] published a significant paper titled "A model for crack initiation in elastic/plastic indentation fields" describing a crack initiation model for indentation. They used a simple approximation for the tensile stress distribution in an elastic/plastic indentation field to determine the critical condition at which crack propagation would occur. Figure 3.3 shows the indenter geometry and nomenclature used in their model.

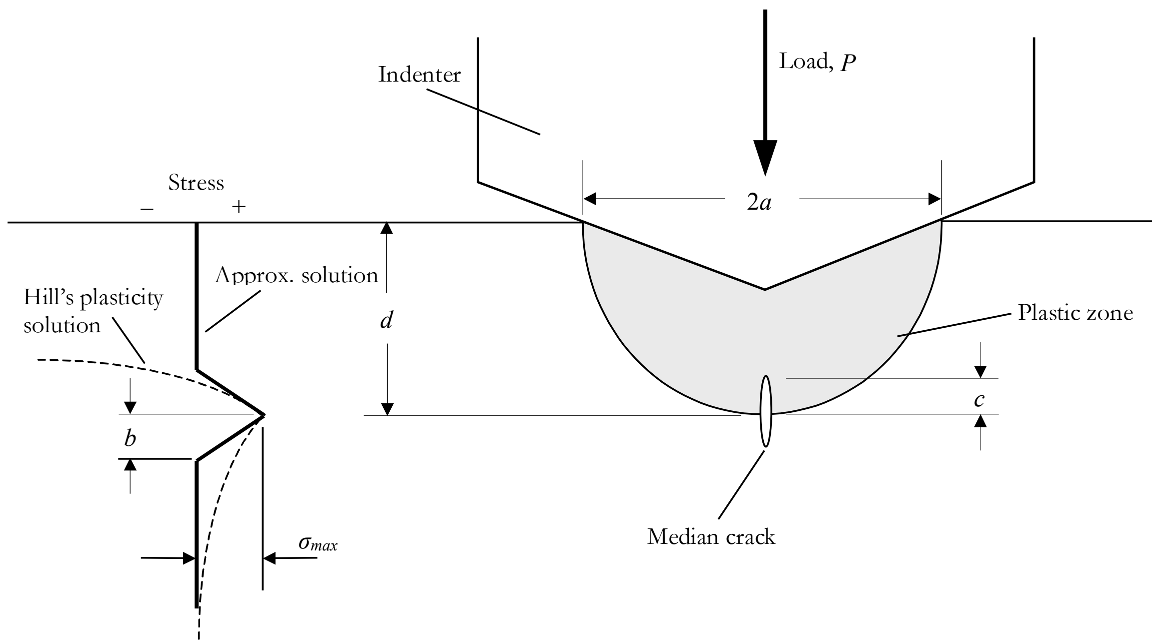

Figure 3.3: Indentation geometry and simplified stress distribution for median crack initiation in an elastic/plastic indentation field after Lawn and Evans [31]. σ_{max} is the max. tensile stress at the elastic/plastic interface, d is the depth of penetration below the surface, and b is the spatial extent over which the tensile component of the stress field acts.

As shown in Figure 3.3, the maximum tensile stress, σ_{max}, occurs at the elastic/plastic interface. Lawn and Evans approximated the features of the Hill's plasticity stress distribution pertinent to the fracture problem as linear functions in the area of maximum tensile stress.

In indentation tests, a sharp indenter with a load P produces a plastic impression of characteristic dimension, a, in the material. Therefore, the hardness, H, is given as

$$H = \frac{P}{\alpha \pi a^2} \tag{3.1}$$

The hardness of the material must scale directly with the indentation pressure (or maximum tensile stress). Similarly, Lawn and Evans noted that the spatial extent over which the tensile field acts should scale with the indentation dimension, a, giving

$$b = \eta a = \eta \left[\frac{P}{\alpha \pi H} \right]^{1/2} \tag{3.2}$$

where η is a dimensionless scaling parameter and α is a dimensionless factor that depends on the indenter geometry. By considering a median-plane crack of radius, c, centered on the load axis at the elastic/plastic interface and invoking the Griffith fracture criterion ($K = K_c$), the critical relations for crack extension can be found. The result of the Lawn and Evan's model is that the minimum flaw size, c_{min}, required from an energy standpoint, to initiate fracture is given as

$$c_{min} = \beta_1 \left(\frac{K_c}{H} \right)^2 \tag{3.3}$$

where β_1 is a dimensionless scaling parameter. From the same analysis, the minimum load required to initiate fracture under the indenter is

$$P_{min} = \beta_2 \frac{{K_c}^4}{H^3} \tag{3.4}$$

where β_2 is another scaling factor.

Although Lawn and Evans used many assumptions in the derivation, the model suggests that fracture toughness and hardness are important material properties in governing fracture in brittle materials. From experimental data, it was found by Lawn and Evans that equation (3.3) produced reasonably accurate results for the minimum indentation depth required to initiate fracture.

In compression tests, Kendall [26] found that as the specimen size approached a critical value, the force required for crack propagation steadily increased. Kendall gives this critical size as

$$d = \frac{32}{3}\frac{E\Gamma}{\sigma_y^{\ 2}} \tag{3.4}$$

where E is the elastic modulus, Γ is the surface fracture energy, and σ_y is the yield stress of the material. At this critical size, crack propagation became less favorable and gross yielding of the specimen occurred.

Other researchers have developed similar models for crack initiation based on the Griffith fracture criteria. Lawn, Jensen, and Arora [32] found that the minimum depth for crack initiation in indentation studies of brittle materials was a function of the material properties and given as

$$d = \xi \frac{E\Gamma}{H^2} \tag{3.5}$$

where ξ is a dimensionless parameter that depends largely on the indentation geometry. Lawn, et. al. used the quantity $H^2/E\Gamma$ as an effective measure of brittleness for any given indentation configuration.

These relatively simple models for the minimum indentation depth and indenter load provide valuable insight into the governing material properties for fracture initiation in machining. Lawn [33] notes that for an anisotropic material, the crystallographic dependence of the elastic parameters (which affect the surface fracture energy, Γ) complicates the issue of predicting fracture because crack propagation will depend on the orientation of the cleavage planes in the stress field as well as the resolved stress along the cleavage planes.

3.2 DUCTILE-REGIME MACHINING

Much of the early research, carried out in the 1970s and early 1980s, in ductile-regime machining focused on understanding the size effects and fracture mechanics issues of the process. It wasn't until the middle to late 1980s that researchers started to investigate machining process parameters such as cutting speed, feed rate, tool nose radius, and tool rake angle.

Syn et. al. [34] used a shoulder analysis technique where the tool was engaged in the workpiece during a facing cut and suddenly retracted leaving an uncut shoulder region where the ductile-to-brittle transition could be analyzed. These researchers used a variety of feed rates and depths of cut in the experiment and found that the ductile-to-brittle transition varied not only with the two experimental variables, but also with crystallographic orientation. The ductile-to-brittle transition depth was found to vary from 0.04 μm to 0.1 μm on the (111) crystal face, but no information on specific crystallographic orientation was given. This study was very important in that it was one of the first published reports that showed the ductile-to-brittle transition could be controlled by varying the feed rate and cutting in a specific crystallographic orientation.

After the early work by Syn et. al. at LLNL, researchers at North Carolina State University began a large research effort to better understand the machining process variables involved in ductile-regime machining. Bifano et. al. [35] developed a critical depth of cut model for ductile-regime grinding of brittle materials. The model used a fracture mechanics approach along with experimental grinding data to determine the critical chip thickness for plunge grinding. The critical chip thickness was found to scale with the material properties pertinent to crack initiation.

$$d_c \, \alpha \left(\frac{E}{H}\right)\left(\frac{K_c}{H}\right)^2 \qquad (3.6)$$

Good qualitative agreement between experimental and analytical results with a wide variety of brittle materials was observed. One disadvantage of Bifano's model is that it assumes an isotropic material with bulk material properties; thus, it does not contain any pertinent crystallographic orientation effects associated with anisotropic materials.

At about the same time of Bifano's work in ductile-regime grinding, other research efforts were being carried out at NC State in ductile-regime turning of brittle materials. Blake et. al. continued the work started by Syn, et. al. at LLNL by studying the ductile-to-brittle transition using the shoulder analysis technique on a parallel-axis diamond turning lathe equipped with a PZT stack to control tool position [36]. This research focused on understanding the ductile-to-brittle transition as a function of machine parameters (feed rate and cutting speed) and tool geometry (rake and clearance angle). Blake's work showed that the critical chip thickness in turning varied as a function of feed rate, tool geometry, and crystal orientation, but was relatively insensitive to cutting speed. In addition, it was shown experimentally that as the rake angle became more negative, the resulting critical chip thickness increased. This negative rake angle effect was attributed to a favorable increased compressive stress ahead of the tool tip.

Blake et. al. defined the critical chip thickness as the thickness of the chip where damage left by previous tool passes could no longer be removed by subsequent tool passes because the machining damage extended below the machined surface plane. A schematic representation of the chip geometry for Blake's model is shown in Figure 3.4.

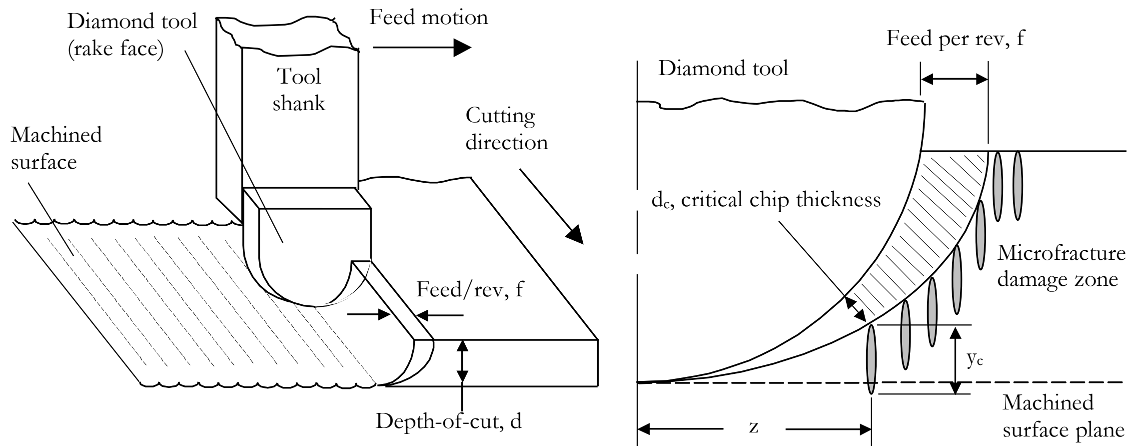

Figure 3.4: Schematic representation of chip formation and machining damage after Blake et. al. [36]. The critical chip thickness is defined as the chip thickness at which subsequent tool passes are unable to remove damage from the previous tool passes.

Although Blake noted that the pitting damage was crystallographic dependent, the critical chip thickness was not measured as a function of crystal orientation. Depending on selection of the machining variables, the critical chip thickness was found to vary from 0.01 μm to 0.2 μm on the (001) silicon crystal face.

Morris et. al. [37] explained that the variation of critical chip thickness with machining parameters in silicon and germanium was due to a high-pressure phase transformation causing a change in material ductility. They concluded that the high pressure under the cutting tool causes a transformation of the diamond-cubic structure to a metallic (β-tin) phase. The pressure beneath the tool will differ with rake angle, feed rate, and material properties (crystal orientation) thus causing a variation in critical chip thickness with all the aforementioned variables.

Instead of using a facing-cut method, Brinksmeier, et. al [38] used a plunge-cut approach to investigate the ductile-to-brittle transition in monocrystalline silicon. In this work, a diamond turning machine was used in a planar arrangement to make an inclined cut at a low cutting speed (20 mm/min) while measuring the cutting and thrust forces. This work

was important because four regimes of material removal in silicon as well as the corresponding force signatures for each regime were identified. Figure 3.5 shows a schematic of the four different regimes of material response in machining silicon.

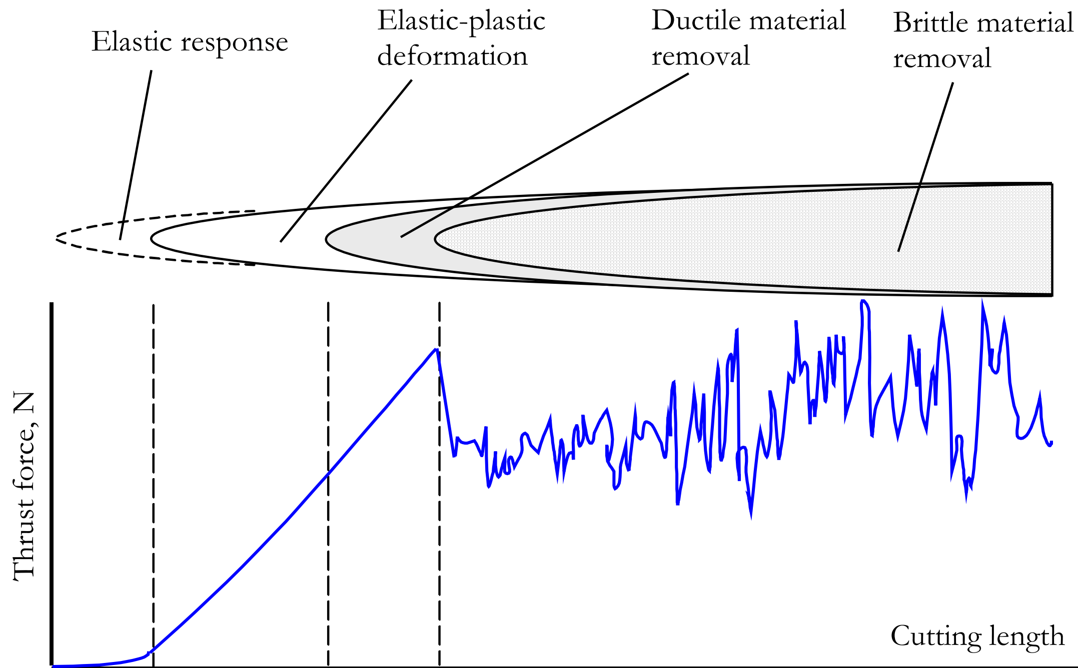

Figure 3.5: Schematic of the four different regimes of material response in a plunge-cut made in monocrystalline silicon after Brinksmeier et. al [38].

The elastic response regime is governed by a steady increase in the thrust force without any trace of surface damage. In the elastic-plastic regime, the thrust force continues to increase, but without visible change in surface topography. As the tool approaches the ductile-to-brittle transition, the thrust force reaches a local maximum. In the brittle regime, the thrust force per unit volume of material removed decreases with random variations in the force caused by the fracture process.

Brinksmeier's approach could easily be adapted to explore a variety of crystallographic orientations in a material without damage from previous tool passes affecting the current cut; however, the tests would be very time consuming.

Blaedel et. al. notes there are two ways to apply ductile-regime machining in practice [39]. One way is to limit the machining force to be less than the force required to initiate and propagate damage into the workpiece. This is more easily done in turning than in grinding, but still poses significant problems. If the force is used as the control variable, than it is very difficult to machine a workpiece to the desired geometry. However, it is important to discern the relative magnitudes of the machining forces because they do give an indication of ductile or brittle-mode machining.

The other, and more practical, approach is to control the chip thickness during machining. This approach is becoming more realizable as machine tools with very low error motions and high structural loop stiffness are readily available. Chip thickness is easily implemented as a ductile-regime machining control variable by regulating the feed rate, spindle speed, and tool geometry.

3.3 CRYSTALLOGRAPHIC ORIENTATION EFFECTS

Early research at LLNL and North Carolina State revealed that the pitting damage left from facing cuts on silicon showed preferential crystallographic patterns. Many attempts at modeling the effect of crystallographic orientation by using metrics such as surface finish, resolved tensile and shear stress, and machining damage have been proposed. A few of these crystallographic models are discussed here.

Blackley and Scattergood [40] used a line force stress model to predict the variation of damage on the various crystal faces of a germanium wafer. The line-force model proposed by Blackley and Scattergood is shown in Figure 3.6.

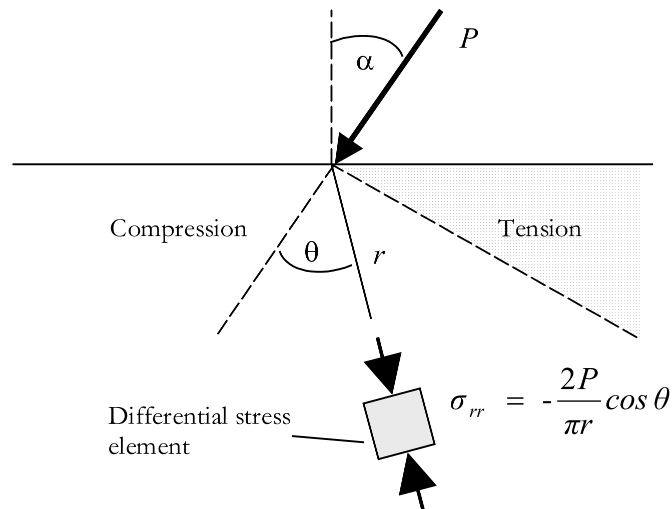

Figure 3.6: Line-force acting on an elastic half-space after Blackley and Scattergood [39] to model crystallographic dependent damage. In polar coordinates, the only nonzero stress component is the radial stress, σ_{rr}, acting a distance r from the point of load application.

Blackley and Scattergood used stress and rotation transformations to calculate the maximum normal stress on the {111} slip planes for a given cutting direction and crystal face. An example of the maximum normal stress and corresponding pitting damage produced by a 0° rake tool on the (001) crystal face is shown in Figure 3.7.

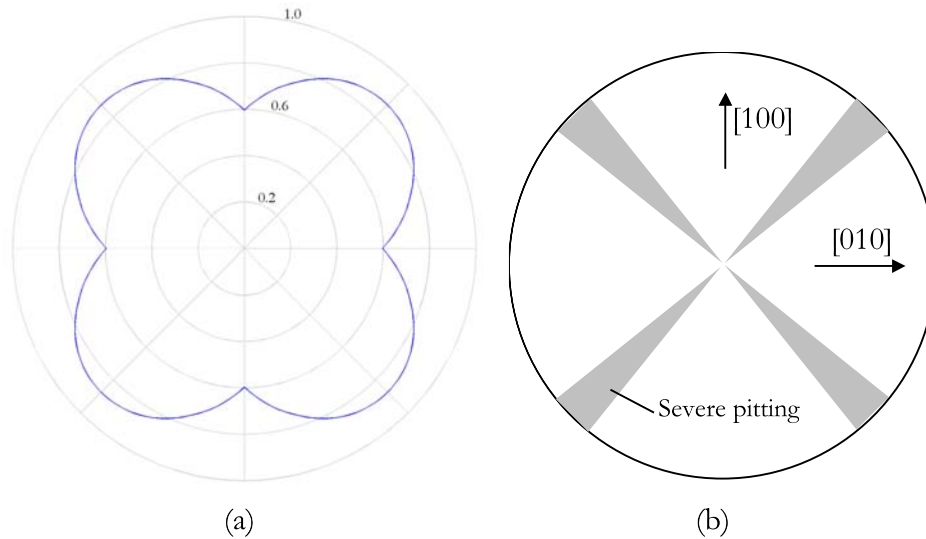

Figure 3.7: (a) Maximum normalized tensile stress as a function of crystallographic orientation on the (001) crystal face after Blackley and Scattergood [40]. (b) Pitting damage on a machined (001) germanium wafer.

In addition to the good qualitative agreement between analytical and experimental results, the simulation helped to support earlier work by Blake et. al. [36] in that negative rake angles were beneficial to ductile-regime machining. Figure 3.8 shows how the maximum normalized tensile stress varies with rake angle on the (001) crystal face of germanium.

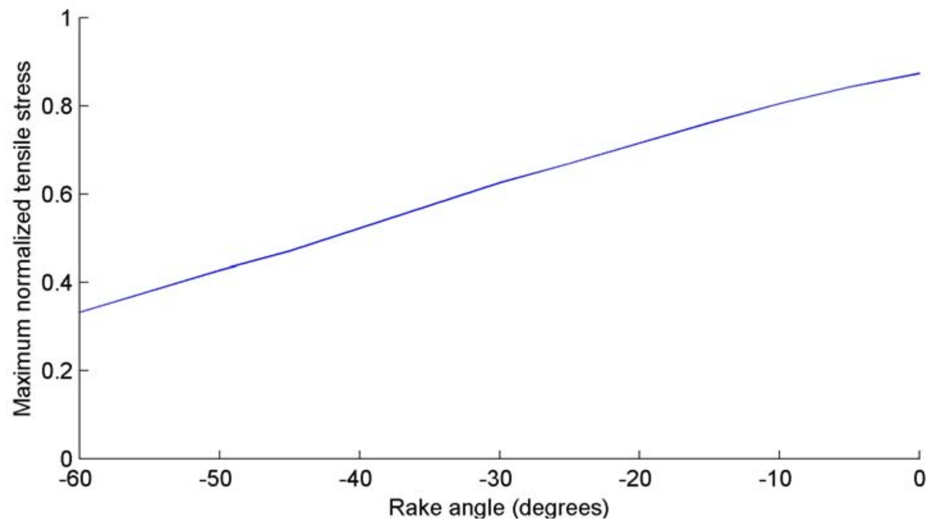

Figure 3.8: Variation of maximum normal stress with rake angle for a (001) germanium wafer.

Shibata et. al. [41] noticed the same pitting damage from turning silicon as previous researchers and was able to qualitatively explain the damage effects by the use of a slip model. Other researchers found that the average roughness of the machined surface varied with crystallographic orientation [42, 43].

It is, therefore, the goal of this research to empirically obtain the critical chip thickness and machining forces as a function of crystallographic orientation on the (001) silicon face. With the knowledge of critical chip thickness and machining forces, the optimum tool geometry and machining direction can be selected.

CHAPTER 4

EXPERIMENTAL TEST SETUP

In this chapter, the machine setup used in the silicon flycutting experiments is discussed. In addition, some qualifying test results are presented that validate the machine's high structural loop stiffness and high accuracy design.

4.1 EXPERIMENTAL TEST BED DESIGN

The silicon flycutting tests are performed on a CNC Moore Nanotech 150AG. The machine, originally designed to grind aspheric lenses, was reconfigured to investigate the effect of crystallographic orientation in silicon flycutting. A solid model of the machine is shown in Figure 4.1.

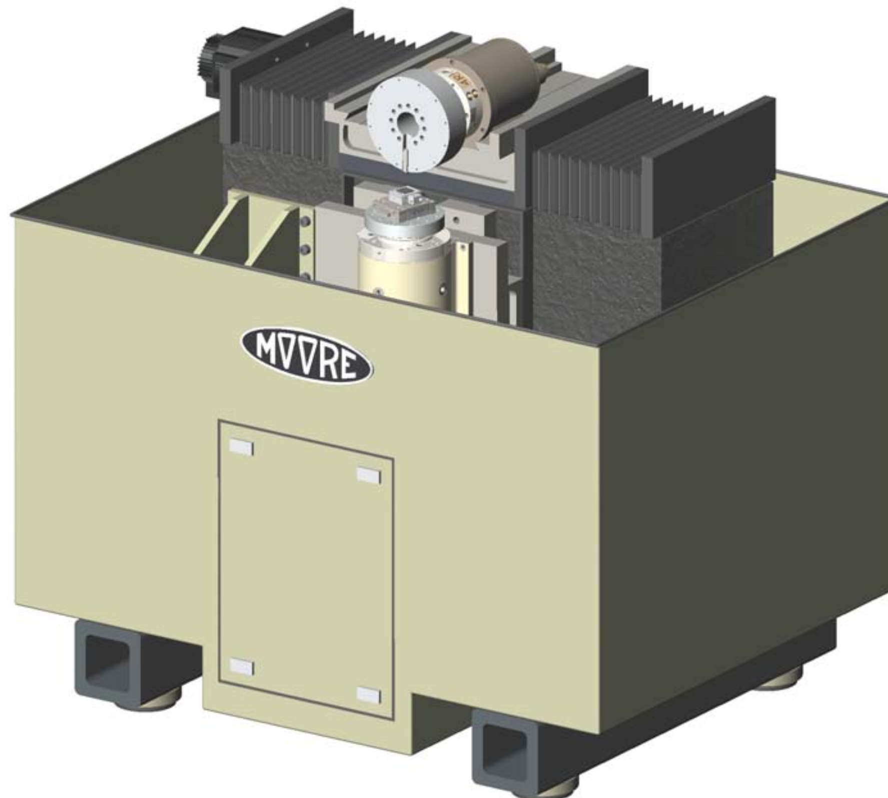

Figure 4.1: Experimental setup for silicon flycutting on a Moore Nanotech 150AG.

The Moore Nanotech 150AG is a two axis (X and Z) machine with hydrostatic slideways. The machine is controlled by an Aerotech U600 PC-based motion controller. Both axes have Heidenhain LIP-401R scales as the feedback device and with external electronic multiplication, a 10 nm linear resolution is achieved. The x and z axes are leadscrew driven with DC brushed motors and have 7,500 counts/rev. rotary encoders which act as tachometers to close the velocity loop. Figure 4.2 shows a zoomed view of the critical components of the test setup.

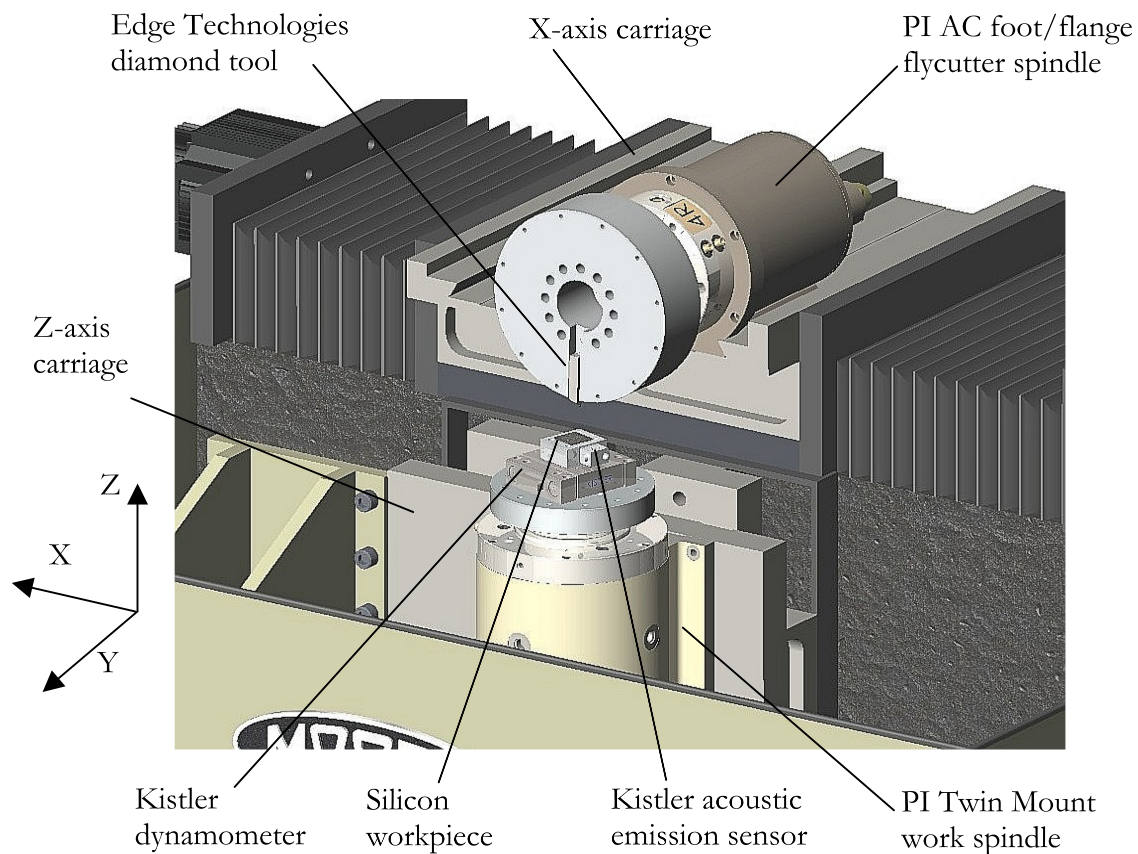

Figure 4.2: Close-up view of the flycutter spindle, workpiece spindle, and instrumentation.

The work spindle, mounted on the z-axis, is a Professional Instruments (PI) Twin Mount air bearing spindle with an Aerotech S-130 brushless DC motor and BAL40-20 linear amplifier. The spindle is equipped with a Heidenhain ERO1384 4096 count rotary encoder.

With an external electronic multiplier, the effective angular resolution of the work spindle is 1.6 arcseconds. This spindle is capable of speeds as low as 0.1 rpm and as high as 700 rpm.

A Kistler Minidyn 9256A2 dynamometer, Kistler 8152B acoustic emission sensor, and workpiece chuck are mounted on the PI Twin Mount work spindle. Figure 4.3 shows a picture of the work spindle and instrumentation layout.

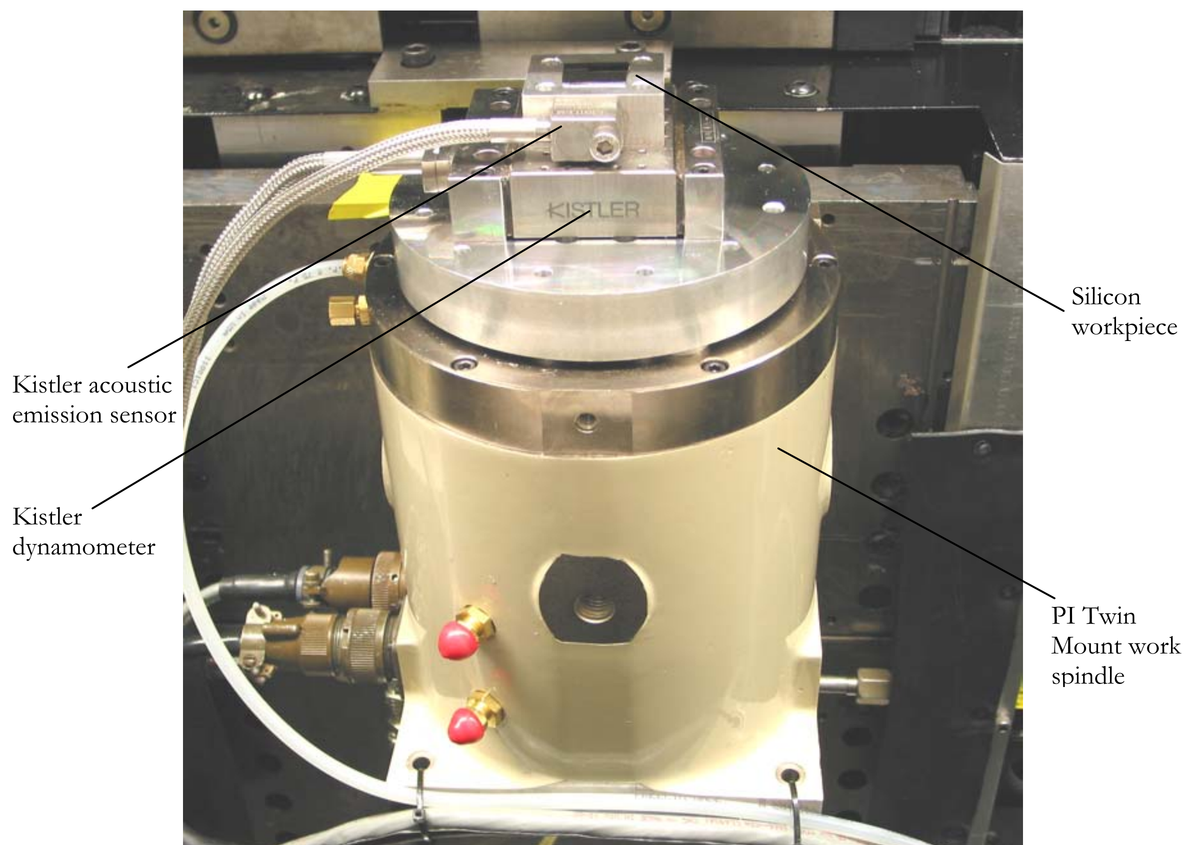

Figure 4.3: Close-up view of the PI Twin Mount work spindle with Kistler dynamometer, Kistler acoustic emission sensor, chuck, and silicon workpiece.

The Kistler Minidyn 9256A2 dynamometer is capable of high-bandwidth, 3-axis force measurements with milli-Newton force resolution and good thermal stability. The Kistler 8152B acoustic emission sensor is used to detect tool-workpiece contact. By monitoring the output of the acoustic emission sensor on an oscilloscope during touch-off, depths of cut on the order of 0.1 micrometers are achieved.

The flycutter spindle, mounted on the x-axis, is a Professional Instruments AC Foot/Flange air bearing spindle. The spindle uses a model 4R Blockhead with an integral 750 Watt (1 hp) AC induction motor. Speeds up to 10,000 rpm are possible. The AC Foot/Flange spindle also exhibits nanometer-level axial and radial error motions. Figure 4.4 is a close-up view of the flycutter spindle, flycutter, and diamond tool.

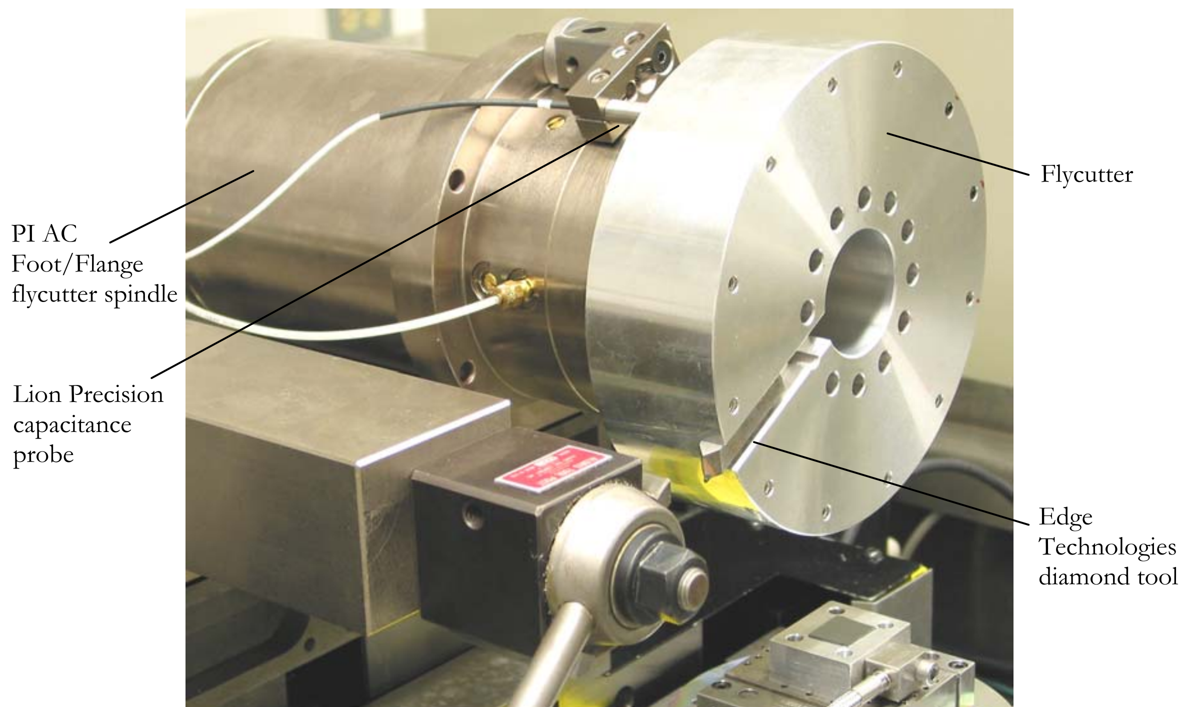

Figure 4.4: Close-up view of the AC foot/flange flycutter spindle mounted on the x-axis.

A Lion Precision capacitance probe (DMT-10 C1, 2.5 μm/volt sensitivity), targeting the back of the flycutter, is used as a data acquisition trigger. Just before the tool comes in contact with the workpiece, a mark on the back of the flycutter passes under the capacitance probe, triggering data acquisition. This data collection technique is used to minimize the resultant file size and maintain high data capture rates.

The diamond tools used in the flycutting experiments are Edge Technologies synthetic monocrystalline diamond tools. The rake and clearance faces are chemically polished which make them ideal for high precision diamond turning applications.

4.2 FLYCUTTING GEOMETRY

The experimental setup allows for small, non-overlapping cuts to be made in a single test in a variety of crystallographic directions. Figure 4.5 illustrates the geometry and kinematics of the machine layout and tool/workpiece interaction during cutting.

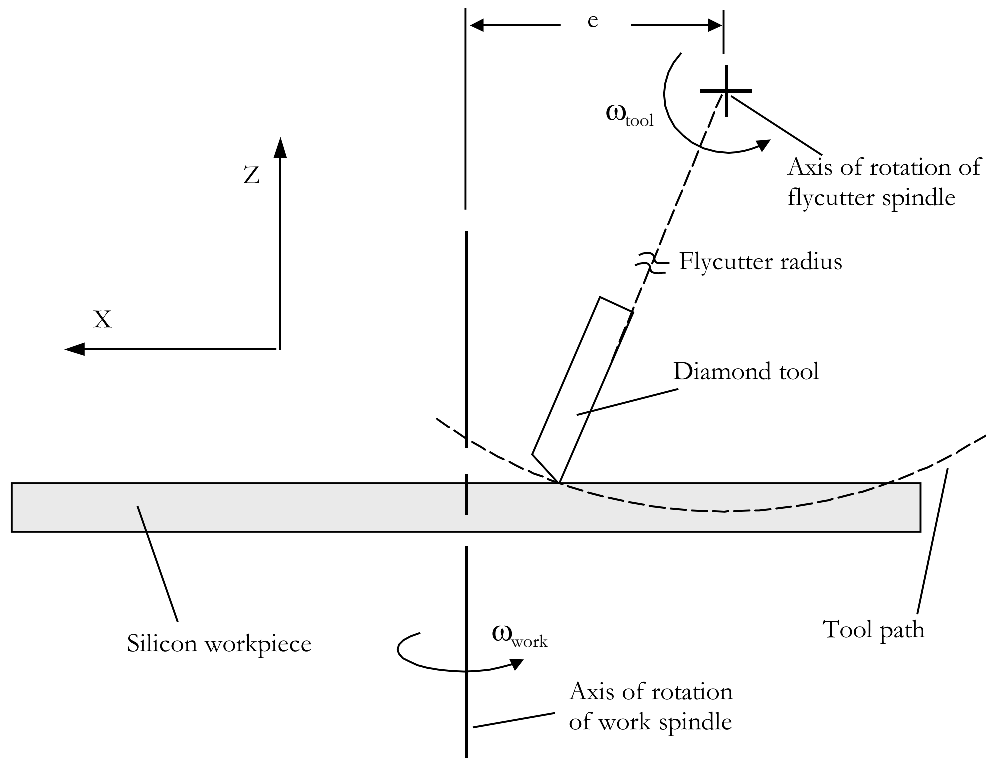

Figure 4.5: Schematic of the flycutter and workpiece geometry for the silicon flycutting tests. The experimental setup allows for a varying chip thickness over a variety of crystallographic directions in a single test.

Since the tool path is an arc, the chip thickness varies during each individual cut. The continually varying chip thickness allows the critical chip thickness to be measured as the depth where ductile material removal changes to brittle fracture.

Since the axis of rotation of the flycutter and the axis of rotation of the work spindle are offset by a distance e, the cuts are made in a circular pattern around the (001) crystal face. For all tests, the flycutter rotates at 120 rpm while the workpiece rotates at 0.6 rpm, allowing for non-overlapping cuts every 1.8 degrees. The machined workpiece contains information

about the critical chip thickness as a function of crystallographic orientation on the (001) crystal face. Figure 4.6 shows an example of a machined workpiece.

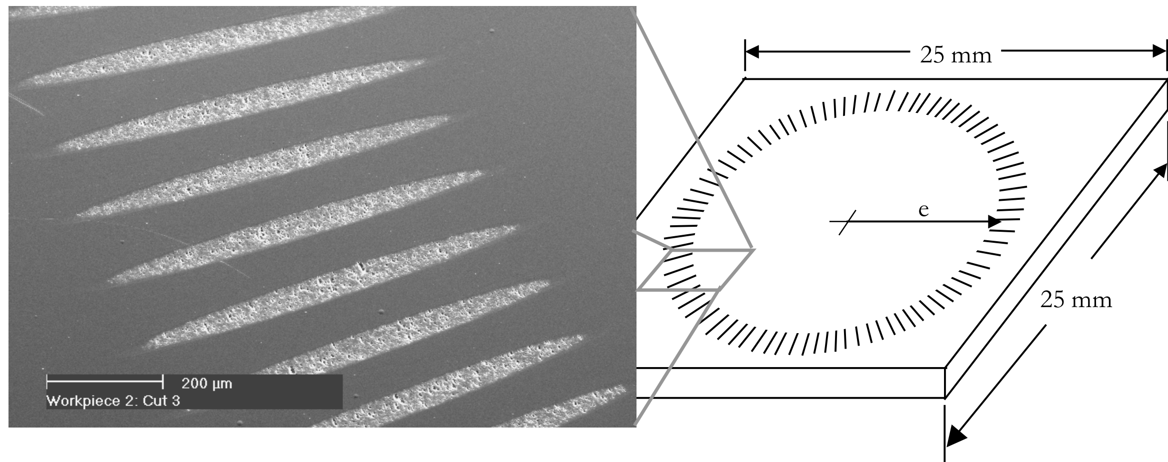

Figure 4.6: Example of the cuts made on the (001) crystal face of monocrystalline silicon by the silicon flycutting setup. The SEM micrograph is a zoomed view of a few cuts.

By using the proposed two-spindle approach, the critical chip thickness and machining forces can accurately be measured over the entire crystal face. Another advantage is that tool track length is minimized; making tool wear insignificant over the course of a single test. In addition, the flycutting tests are insensitive to workpiece flatness because the depth of each individual cut is measured after machining.

4.3 MACHINE METROLOGY

The high-accuracy design of the Moore Nanotech 150AG is important to the success of the silicon flycutting experiments. As previously mentioned, the critical chip thickness in silicon is on the order of 100 nanometers. In order to experimentally measure the critical chip thickness, depths of cut on the same order of magnitude are necessary. Therefore, the machine must be able to take small, repeatable depths of cut to characterize the extremely small critical chip thickness encountered in silicon.

Tests are performed to measure the characteristics of the z-axis important to silicon flycutting. In these experiments, a Lion Precision capacitance probe (DMT-10 C1, 2.5 μm/volt sensitivity) is mounted on the x-axis targeting the workpiece chuck on the z-axis work spindle. This arrangement is representative of the z-axis motion the diamond tool is exposed to during machining. Figure 4.7 shows the experimental metrology test setup.

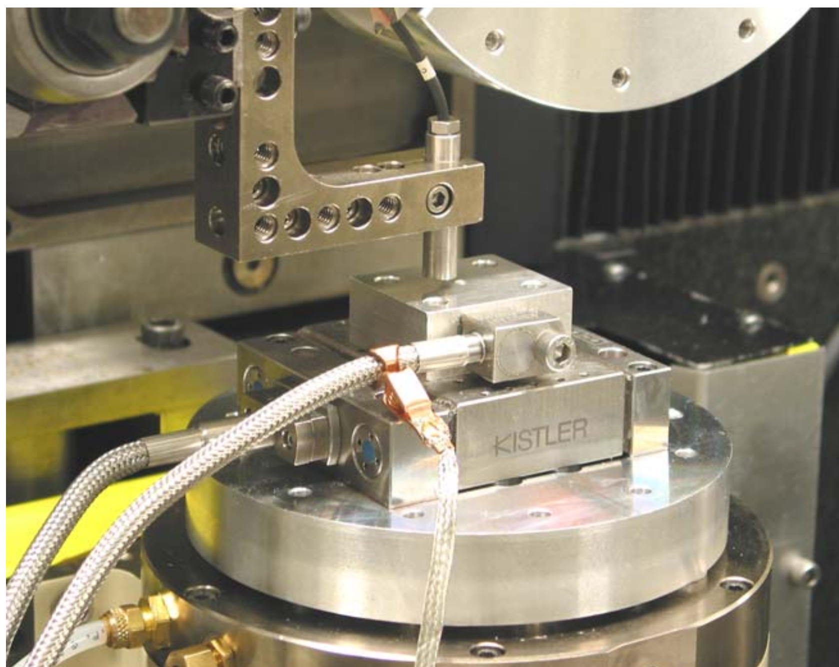

Figure 4.7: Metrology test setup for measurement of z-axis step performance, z-axis repeatability, and z-axis in-position dither.

The first set of performance tests measures the ability of the z-axis to make sub-micrometer steps. The z-axis is commanded to make two steps towards the capacitance probe with a five second pause between each step. By stepping closer to the capacitance probe, the touch-off process is simulated. Figure 4.8 shows the results for commanded steps of 0.25 micrometer (10 microinches) and 1.25 micrometers (50 microinches).

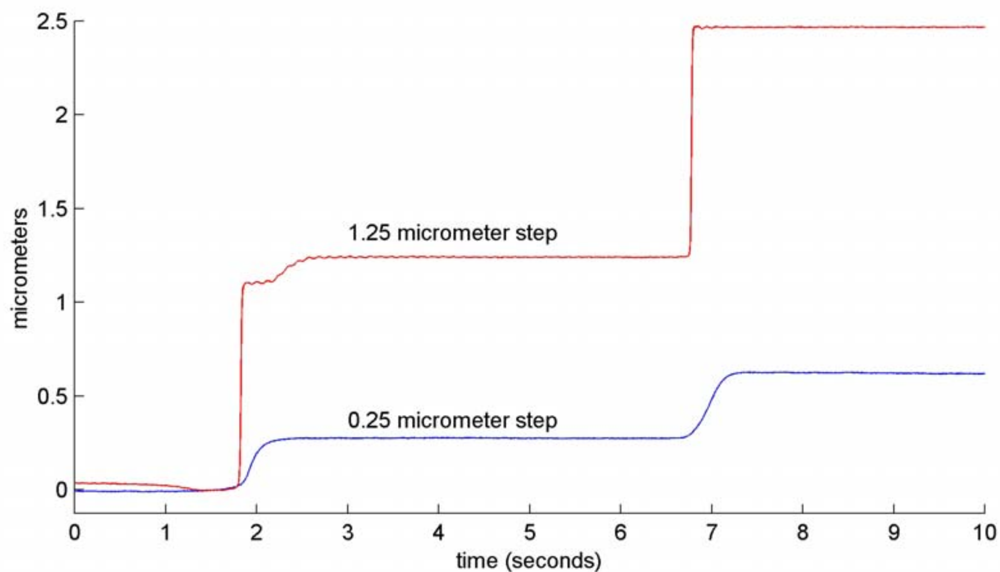

Figure 4.8: Z-axis step tests for 0.25 micrometer and 1.25 micrometer commanded steps.

These tests show the ability of the z-axis to make sub-micrometer moves with very little overshoot. This is a very important attribute when attempting to characterize the critical chip thickness in silicon.

The next series of tests measures the unidirectional repeatability of the z-axis. Between tests, the z-axis must be stepped away from the tool to mount a new workpiece. It is important for the z-axis to be able to return to a position that is just a few micrometers away from tool-workpiece contact.

For these tests, the capacitance probe is zeroed against the workpiece chuck. The z-axis is moved 25 mm away from the capacitance probe, then back towards the probe. This

process is repeated ten times and simulates changing the workpiece. Figure 4.9 shows the results of ten consecutive measurements.

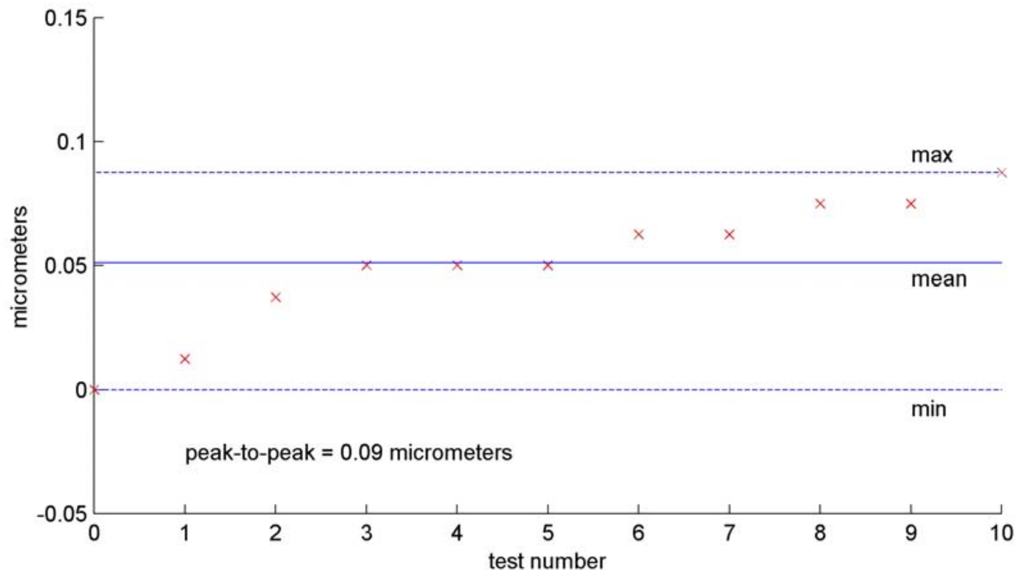

Figure 4.9: Z-axis unidirectional repeatability tests, 25 mm step away and back towards the capacitance probe.

The total time needed to take the ten measurements shown in Figure 4.9 is around ten minutes. Over this time frame, thermal effects may cause the linear drift seen in Figure 4.9. Before this test was performed, the machine had been running for approximately one hour.

According to the ANSI/ASME B5.54-1992 standard *Methods for Performance Evaluation of Computer Numerically Controlled Machining Centers*, the unidirectional repeatability of an axis is defined as the maximum data point less the minimum data point for at least ten measurements [44]. This test shows that the z-axis has a unidirectional repeatability of 0.09 micrometers.

The final test is performed to determine the ability of the z-axis to hold position. During flycutting, it is very important for the z-axis to hold position so that the variation in the depth of cut is minimized. For this test, the z-axis and c-axis servo drives are enabled. Data are collected for a sixty second time period because it is representative of the length of a single flycutting test. Figure 4.10 shows the in-position dither of the z-axis.

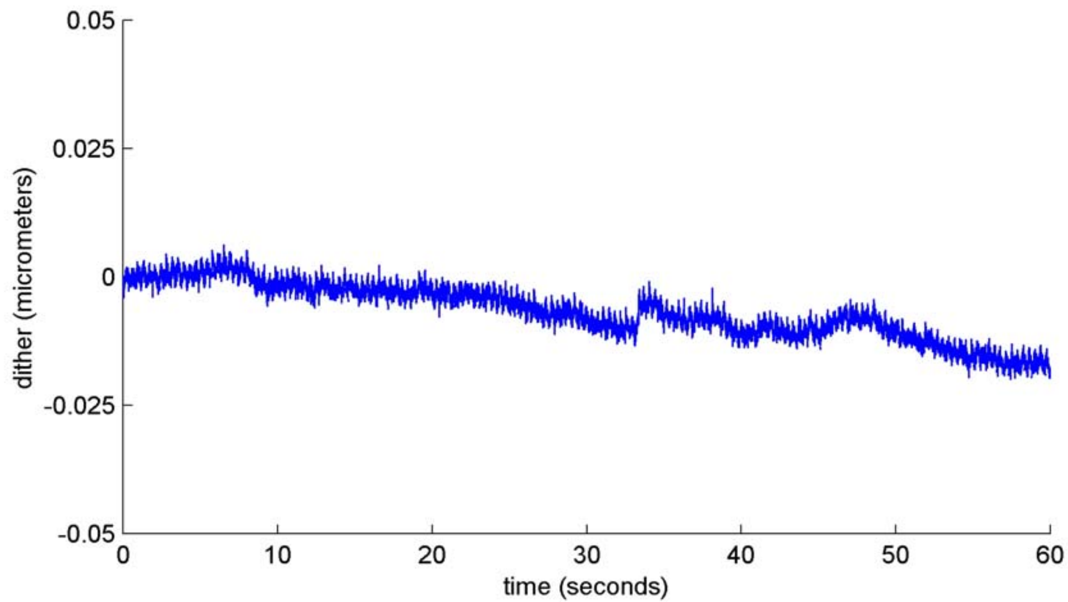

Figure 4.10: Z-axis dither measured with both the z-axis and c-axis servo drives enabled.

Again, a slight linear drift in the data is measured and is likely due to thermal effects. Further inspection of the data indicates the presence of a periodic frequency of approximately 10 Hz. This was determined to be a slight instability in the c-axis, and was corrected by careful tuning of the servo loop. The 10 Hz dither was completely eliminated before any flycutting tests were performed.

4.4 MACHINE DYNAMICS

In order to understand the dynamics of the flycutting test-bed and the limitations of the instrument, an experimental modal analysis is conducted. The structure is excited using a 2000 N Kistler modal hammer (Model #9724A2000) while the response is measured at 68 points using a ±5 g Kistler tri-axial accelerometer (Model #8690C5). A Siglab dynamic signal analyzer (Model #50-42) with a Boxcar window and 500 Hz bandwidth is used to collect the frequency response functions at the modal test points. The data are then post-processed using STAR Modal software to obtain the natural modes of vibration. Figure 4.11 shows the undeformed experimental modal grid of the Moore Nanotech 150AG.

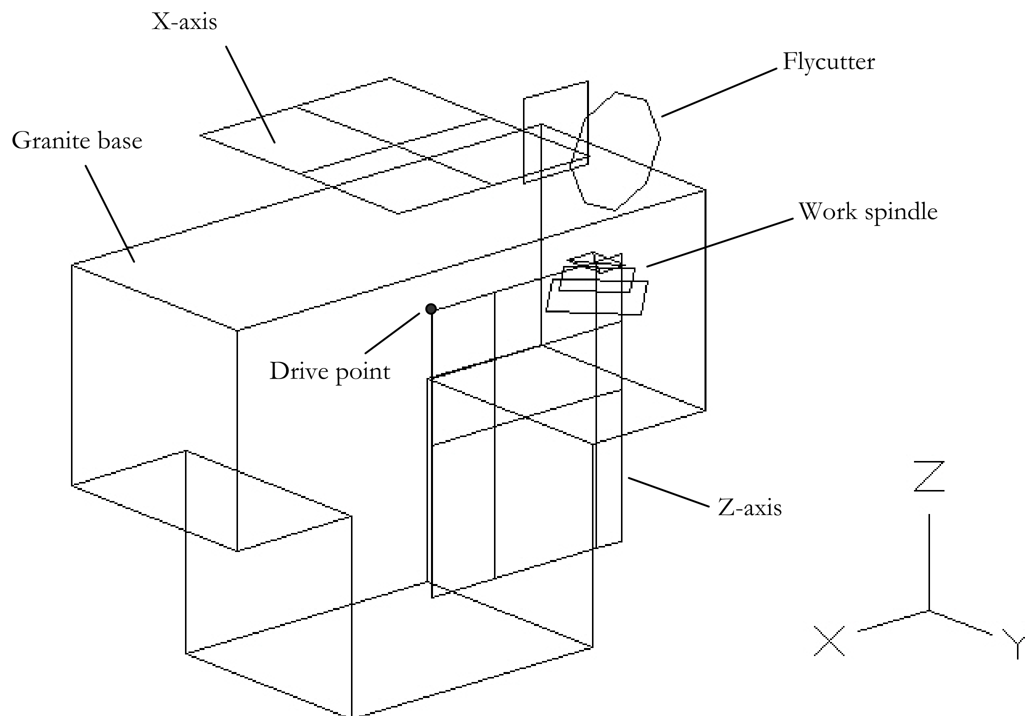

Figure 4.11: 68-point undeformed experimental modal test grid of the Moore 150AG.

After performing an extensive modal pretest, the drive point location was chosen to be on the top of the z-axis. Figure 4.12 shows the drive point frequency response function.

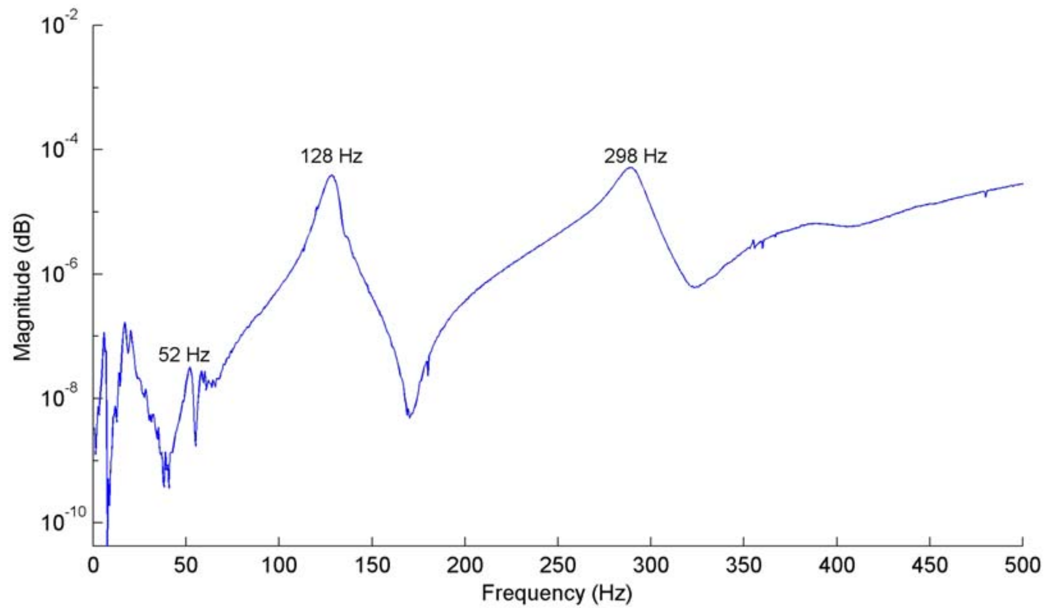

Figure 4.12: Drive-point frequency response function.

The highest rigid body mode of the Moore Nanotech 150AG occurs at 52 Hz. The granite base of the machine is supported by a steel frame, which is not included in the modal grid. Rubber pads isolate the granite base from the steel supporting structure. Figure 4.13 shows the 52 Hz mode of the base bouncing on the steel support frame.

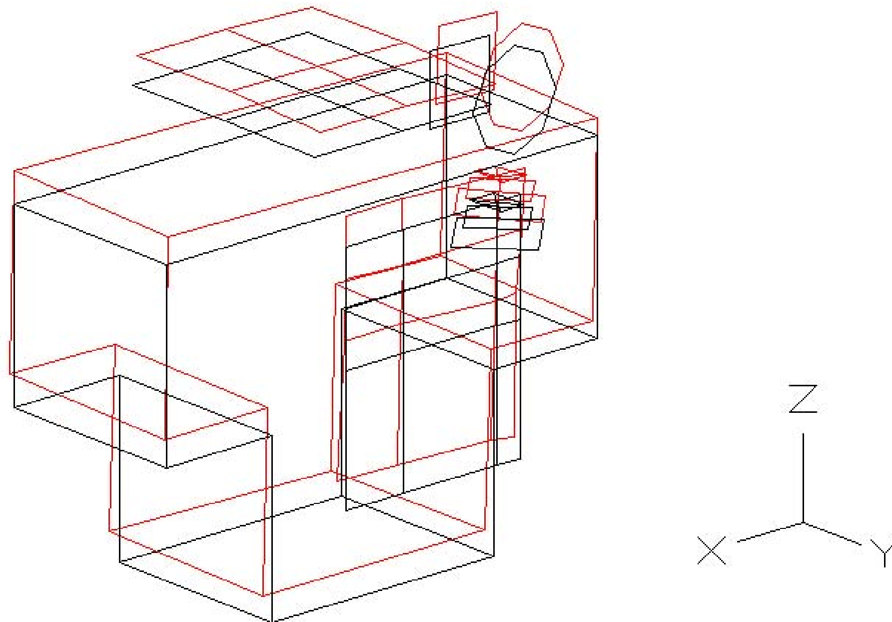

Figure 4.13: Highest rigid body mode of the Moore 150AG occurring at 52 Hz.

The first structural mode of the machine is the z-axis bouncing on the leadscrew assembly at 128 Hz. This mode occurs in the sensitive direction for the flycutting tests, and as a result, limits the bandwidth of the machine. Figure 4.14 shows 128 Hz z-axis mode.

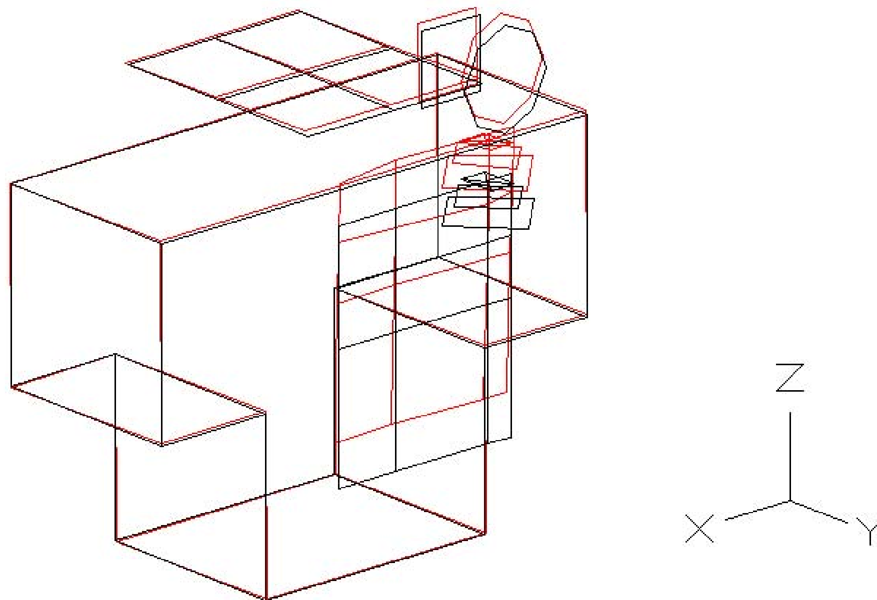

Figure 4.14: The first structural mode of the machine. This mode is the z-axis bouncing on the leadscrew at 128 Hz with 3% damping. This machine mode is the first mode in the sensitive direction during flycutting.

The second structural mode of the Moore Nanotech 150AG occurs at 290 Hz. This mode is largely due to a plate mode of the z-axis, but tilting of the flycutter spindle is also present. The 290 Hz mode also occurs in the sensitive direction for the silicon flycutting tests. Figure 4.15 shows the 290 Hz combined z-axis plate/flycutter tilt mode.

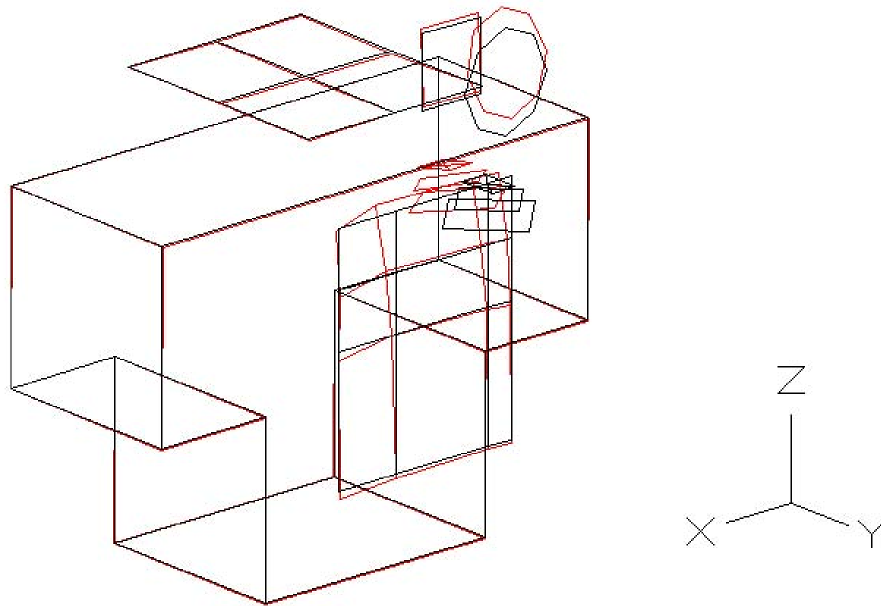

Figure 4.15: The second structural mode of the Moore Nanotech150AG. This mode occurs at 290 Hz with 3% damping. This machine mode also occurs in the sensitive direction for the flycutting tests.

In addition to determining the natural modes of vibration of the Moore Nanotech 150AG, the dynamic compliance between the tool and workpiece is measured. The static stiffness of a machine tool is extremely important; however, the dynamic stiffness, which governs the dynamics of the machining process, cannot be overlooked.

For this test, the dynamic compliance between the flycutter and the workpiece chuck is measured in the sensitive (Z) direction. An accelerance frequency response function is measured between the workpiece chuck (point 1) and flycutter (point 2). The workpiece chuck is excited by an impact hammer and the response is measured with an accelerometer at the flycutter. The accelerance frequency response function, $A_{12}(\omega)$, is then transformed to a compliance frequency response function, $H_{12}(\omega)$, by using equation (5.1).

$$H_{12}(\omega) = -\frac{1}{\omega^2} A_{12}(\omega) \tag{5.1}$$

The resultant cross point compliance between the flycutter and the workpiece is shown in Figure 4.16.

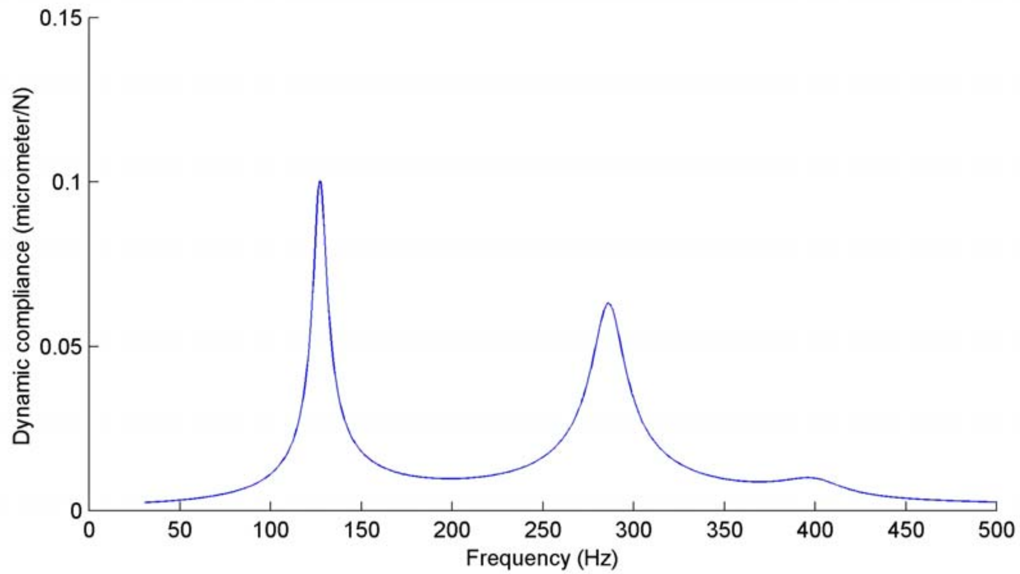

Figure 4.16: Cross point compliance measurement, $H_{12}(\omega)$ in the sensitive (Z) direction between the flycutter and workpiece chuck.

Both of the first two structural modes of the machine (128 Hz and 290 Hz) occur in the sensitive (Z) direction. As a result, both modes show up as larger sources of compliance in the structural loop.

CHAPTER 5

EXPERIMENTAL PROCEDURE

This chapter overviews the experimental procedure used for the silicon flycutting experiments. The procedure used to prepare the machine and workpieces for flycutting is also discussed. In addition, the microscopy techniques used to quantify the critical chip thickness and inspect the workpieces are presented. Finally, the methods used for data post-processing are reviewed.

5.1 MACHINE AND WORKPIECE PREPARATION

Before the flycutting experiments are performed, some machine and workpiece preparation is necessary. In order to achieve predominantly ductile cuts around the entire crystal face, the workpiece circular flatness must be much less than one micrometer.

To achieve the highest degree of accuracy of the mounting surface, the mounting plate and workpiece chuck are diamond turned in place after mounting. The circular flatness of the diamond turned chuck is measured with a capacitance probe and found to be less than 100 nanometers.

The individual silicon workpieces are made from polished 150 mm (001) n-type silicon wafers. The workpieces are cleaved from the 150 mm wafer such that the sides of the workpiece are referenced to the [110] crystallographic direction. Figure 5.1 shows an illustration of a typical silicon workpiece made from a 150 mm wafer.

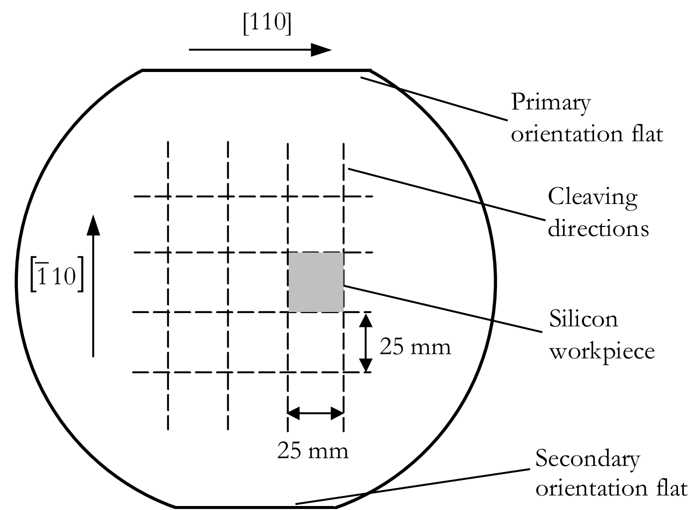

Figure 5.1: Typical 25 mm by 25 mm silicon workpiece made from a polished 150 mm (001) n-type silicon wafer.

The silicon workpieces are mounted to the workpiece chuck with Loctite® 425 adhesive. The circular flatness of the silicon workpiece is then measured with a capacitance probe. Typical values of the workpiece circular flatness are between 0.1 and 0.5 micrometers. The workpieces are used in the as-polished state in order to avoid any surface and subsurface damage created by machining the workpieces before flycutting. Since each individual cut is measured after the flycutting tests, absolute flatness is not extremely critical to the success of the experiments; however, care is taken in mounting the workpieces to minimize depth of cut variation.

5.2 SELECTION OF MACHINING VARIABLES

The flycutting tests are performed on the (001) crystal face of silicon. The objective of the tests is to determine the effect of crystallographic orientation on the critical chip thickness and machining forces. This section discusses the types of diamond tools used and the selection of machining speeds.

5.2.1 DIAMOND TOOLS

As previously mentioned in Section 3.2 and 3.3, the tool rake angle plays a significant role in the critical chip thickness. Therefore, tests are performed for rake angles of 0 degrees, -30 degrees, and –45 degrees to investigate the effect of tool rake angle on the critical chip thickness variation in silicon. The nose radius also affects the chip formation process in turning because it will change the chip thickness for a given feedrate and depth of cut [34, 36, 39]. However, the cuts made in these experiments are non-overlapping and closely replicate an orthogonal cutting model. The effect of nose radius on the chip formation process is not investigated in these experiments, however experiments are planned to investigate this effect.

The tools used in the flycutting experiments are Edge Technologies synthetic monocrystalline diamond tools, which have chemically polished rake and clearance faces making them ideal for high precision diamond turning. Table 5.1 shows the properties of the diamond tools used in the flycutting tests.

Table 5.1: Diamond tool properties used in flycutting tests.

Tool	Rake angle (degrees)	Nose radius (mm)	Clearance angle (degrees)
1	-45	0.72	8
2	-30	1.60	7
3	0	1.52	8

5.2.2 Flycutter and Work Spindle Speed

A compromise is made between the selection of flycutter speed and the allowable temperature rise of the spindle. Ideally, the flycutter speed would be low so that the full instrument bandwidth could be realized and many data points would be captured during cutting. However, since a 4-pole AC induction motor drives the flycutter spindle, the optimal speed of this motor is 1800 rpm. Lower spindle speeds cause the motor to draw more current due to an increase in the back emf of the motor. As a result, the flycutter spindle dissipates more heat causing localized thermal deformations. As the spindle speed is increased, the sampling frequency must be increased in order to obtain an adequate number of data points during each cut. By increasing the sampling frequency, the amount of useful force data is reduced because the bandwidth of the instrument is surpassed.

Therefore, all tests are performed with a flycutter spindle speed of 120 rpm. This allows for an adequate number of data points to be sampled during each individual cut as well as keeps the flycutter spindle temperature at a reasonable level. In addition, a spindle speed of 120 rpm corresponds to a cutting speed of 1400 mm/s at the tool tip. This speed is approximately the same cutting speed as other researchers have used [34, 36]. Finally, in order to make a cut at every two degrees around the entire crystal face, a workpiece spindle speed of 0.6 rpm is chosen.

5.3 TESTING PROCEDURE

After the workpiece is mounted, the workpiece spindle is oriented such that the first cut is made in the [110] direction. This provides a crystallographic reference for the force data and workpiece metrology.

Visually, the diamond tool is brought as close to the workpiece as possible. The flycutter spindle is then turned on to 120 rpm and the z-axis is stepped toward the workpiece in 0.25 micrometer increments. While infeeding, the output of the acoustic emission sensor is monitored on an oscilloscope. By using the output of the acoustic emission sensor to detect touch-off, sub-micrometer depths of cut are realized.

Once touch-off is achieved, data acquisition is started. The force output of the Kistler dynamometer is sampled at 51.2 kHz, using the full bandwidth of the Siglab data acquisition system. The data are digitally low-pass filtered during post-processing. The workpiece spindle is commanded to move 350 degrees at a feedrate of 0.6 rpm. By moving only 350 degrees, the starting and stopping point of each test is easily recognized on the workpiece.

After the test is complete, the z-axis is moved away from the tool by 25 mm and a new workpiece is mounted. After a new workpiece is mounted and the circular flatness measured, the z-axis is stepped 24.998 mm back towards the tool leaving the tool and workpiece only a few micrometers away from contact. The infeed process is then repeated.

The same process is repeated until a satisfactory number of tests are performed for a given diamond tool (rake angle). Once the tool is changed, the effective datum point of tool/workpiece contact is lost because the diamond tools can vary in length by a few millimeters. Therefore, the process of visually getting the tool and workpiece as close as possible is repeated after each tool change.

5.4 WORKPIECE METROLOGY

The workpieces are measured using optical microscopy and scanning electron microscopy to characterize the critical chip thickness variation around the (001) crystal face. The critical chip thickness is characterized as the depth of cut where a noticeable change in surface topography (e.g. pitting, cracks, etc.) starts to occur.

5.4.1 CRITICAL CHIP THICKNESS CALCULATION

By measuring a few dimensions of each cut, the critical chip thickness, t_c, is calculated from simple geometry. Figure 5.2 shows the geometry of an individual cut made in a silicon workpiece.

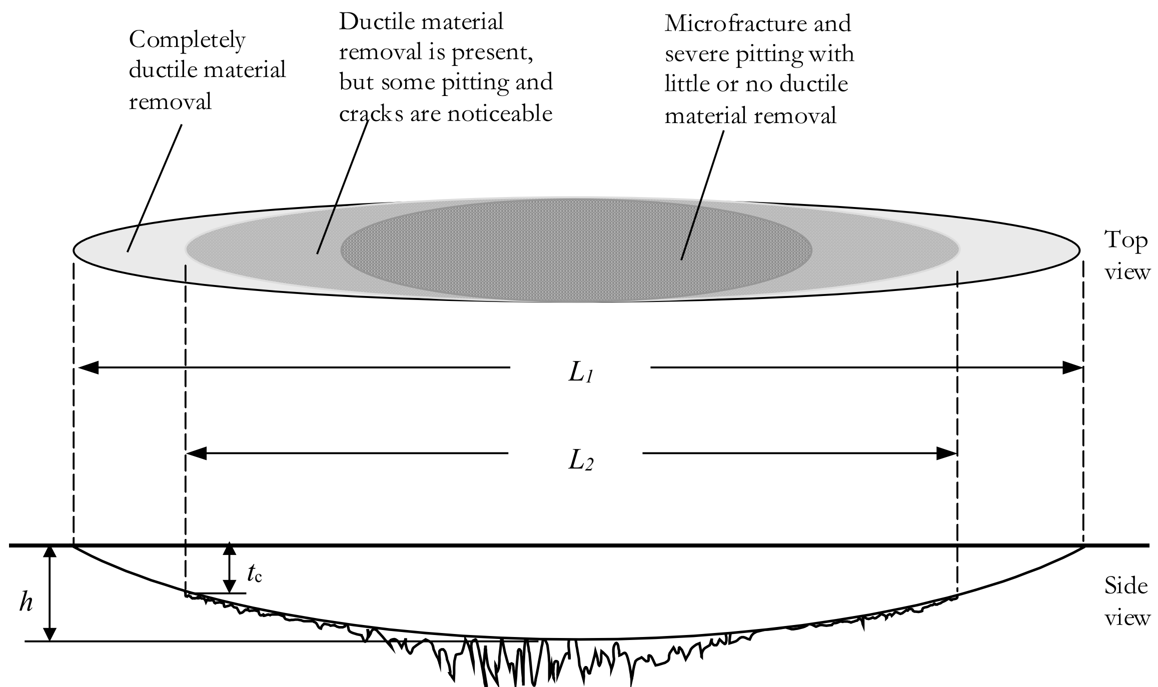

Figure 5.2: The geometry of an individual cut made in a silicon workpiece. The critical dimensions used in the calculation of the critical chip thickness are shown. The length of the overall cut is L_1, the length of the damaged region is L_s, and the depth of cut is h.

Figure 5.3 shows the geometry of an arc of a circle that is used to calculate the critical chip thickness, t_c.

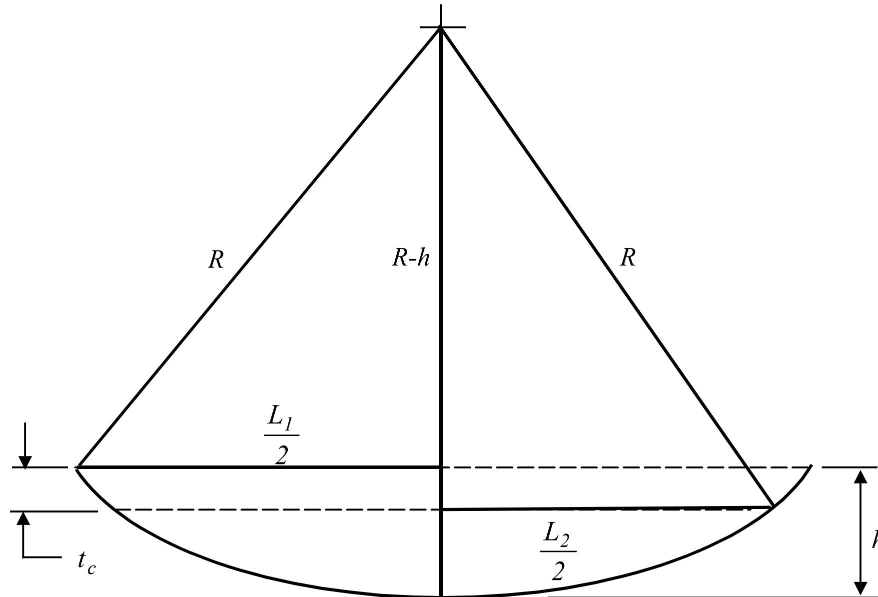

Figure 5.3: Simplified cut geometry used to calculate the critical chip thickness. In this figure, *R* is the flycutter radius and t_c represents the critical chip thickness.

By using the Pythagorean theorem, a relationship between the length of the cut, L_1, flycutter radius, *R*, and the depth of cut, h, is obtained.

$$R^2 = (R - h)^2 + \left(\frac{L_1}{2}\right)^2 \tag{5.1}$$

Simplifying this expression farther yields

$$2Rh - h^2 = \frac{L_1^2}{4} \tag{5.2}$$

Since the depth of cut, h, (on the order of 1 micrometer) is much smaller than the flycutter radius, *R*, (110 mm), the h^2 term can be neglected. Therefore, the depth of cut is calculated as

$$h = \frac{L_1^2}{8R} \tag{5.3}$$

Similarly,

$$R^2 = (R - h + t_c)^2 + \left(\frac{L_2}{2}\right)^2 \tag{5.4}$$

Expanding equation (5.4) yields

$$R^2 = R^2 - 2Rh + 2Rt_c - 2ht_c + h^2 + t_c^2 + \frac{L_2^2}{4} \tag{5.5}$$

By neglecting the small terms (h^2, t_c^2, and $2ht_c$) in equation (5.5) and substituting equation (5.3) for the depth of cut, ***h***, the critical chip thickness is found.

$$t_c = \frac{L_1^2 - L_2^2}{8R} \tag{5.6}$$

By measuring the flycutter radius (R), the length of the cut (L_1), and the length of the damaged region in the cut (L_2), the critical chip thickness is calculated from equation (5.6).

5.4.2 Sensitivity Analysis

In order to determine the effect of uncertainties in the measurement of the critical chip thickness, a sensitivity analysis is performed. The sensitivity of the critical chip thickness to each of the measured variables (L_1, L_2, and R) is calculated by taking the partial derivatives with respect to each variable. The sensitivities are

$$\frac{\partial t_c}{\partial L_1} = \frac{L_1}{4R} \tag{5.8}$$

$$\frac{\partial t_c}{\partial L_2} = -\frac{L_2}{4R} \tag{5.9}$$

$$\frac{\partial t_c}{\partial R} = \frac{L_2^2 - L_1^2}{8R^2} \tag{5.10}$$

By using representative values for L_1, L_2, and R, a numerical value for each of the sensitivities is obtained. For L_1 = 1.0 mm, L_2 = 0.9 mm, and R = 110 mm, the sensitivities are found.

$$\frac{\partial t_c}{\partial L_1} = 2.3 \, x \, 10^{-3} \tag{5.11}$$

$$\frac{\partial t_c}{\partial L_2} = 2.1 \, x \, 10^{-3} \tag{5.12}$$

$$\frac{\partial t_c}{\partial R} = -2.0 \, x \, 10^{-6} \tag{5.13}$$

Equations (5.11) through (5.13) show that the critical chip thickness calculation is much more sensitive to errors in the measurement of the lengths, L_1 and L_2, than the flycutter radius, R. Figure 5.4 shows the contributions of each measured variable to the critical chip thickness uncertainty.

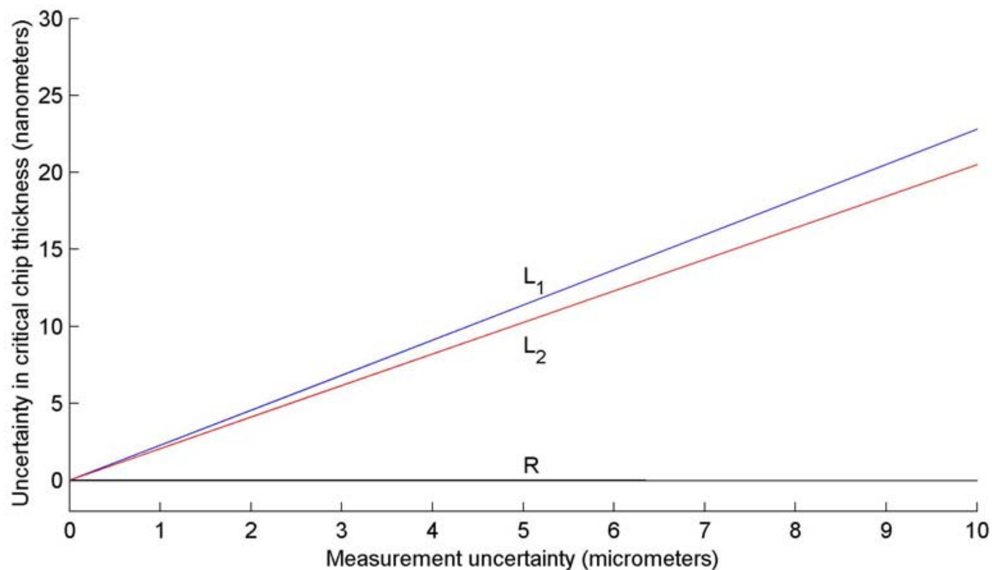

Figure 5.4: Individual contributions of L_1, L_2, and R to the critical chip thickness uncertainty. The uncertainty is calculated for nominal values of the measured variables: L_1 = 1.0 mm, L_2 = 0.9 mm, and R = 110 mm.

5.4.3 OPTICAL MICROSCOPY

An Olympus BX60 Nomarski reflected-light optical microscope with a display is used to measure the machined silicon workpieces. A silicon artifact with 100 micrometer wide etched lines is used to calibrate the microscope display. Twelve centimeters on the display is found to correspond to 700 micrometers on the measured artifact (58.33 micrometers/cm). With this as the calibration standard, the individual cuts are measured under 5x, 20x, and 50x magnification. If a 20x or 50x objective is used during the measurement, the appropriate correction factor is applied to the calibration factor in order to account for the different magnification. An example of a few cuts in silicon approximately 20° from the [100] direction under 20x magnification is shown in Figure 5.5.

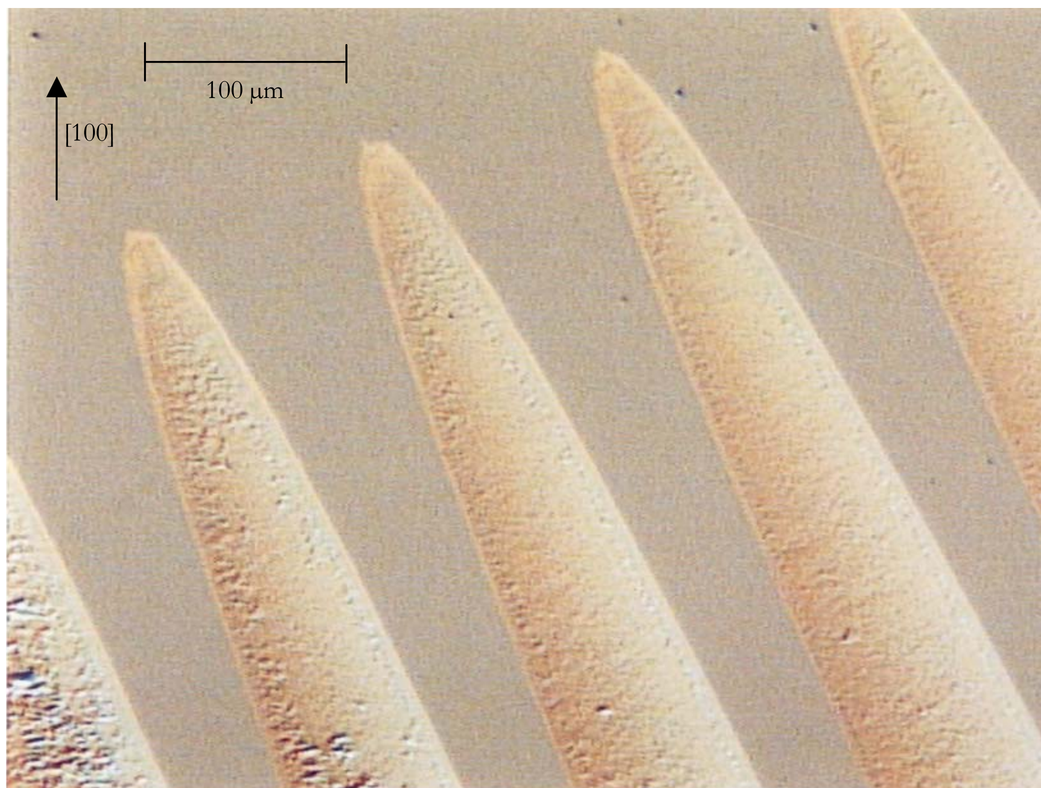

Figure 5.5: Nomarski micrograph of multiple cuts in silicon under 20x magnification. These cuts are approximately 20° from the [100] direction.

5.5 DATA POST-PROCESSING

The force data are captured at a sampling frequency of 51.2 kHz to obtain the maximum number of data points during the actual cut as possible. For a flycutter spindle speed of 120 rpm and a depth of cut of 1 micrometer, the amount of time the diamond tool is in contact with the workpiece during a single cut is approximately 0.5 milliseconds. Therefore, in order to avoid large attenuation of the force amplitude, the data are digitally low-pass filtered at a cutoff frequency of 2000 Hz. Both the thrust force (force normal to the workpiece) and the cutting force (parallel to the workpiece) are measured; however, the cutting force is found to lie in the noise floor of the force data. Figure 5.5 shows an example of a filtered and raw thrust force trace for a single cut made in silicon.

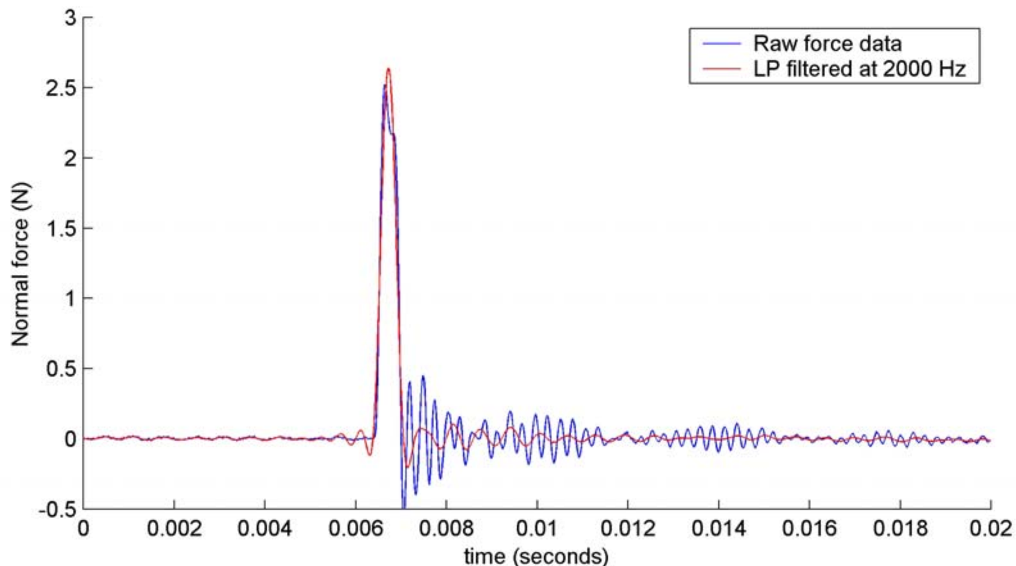

Figure 5.5: Time trace of the filtered and raw thrust force data for a single cut.

From the experimental modal analysis, it was found that the first structural mode in the sensitive direction was 130 Hz. Since the force data is low-pass filtered at 2000 Hz, structural frequencies are not removed. However, by low-pass filtering at the instrument bandwidth of 100 Hz, much of the force data is attenuated.

In order for the test results to be compared for the different tool nose radii, the force data is normalized by the chip area at the deepest part of each cut. This also allows correction for any force variation from the workpiece flatness. The chip area is calculated by simple geometry with the knowledge of the tool nose radius, *r*, and flycutter radius, *R*, and the length of the cut, L_1. Figure 5.6 shows the geometry used to calculate the chip area.

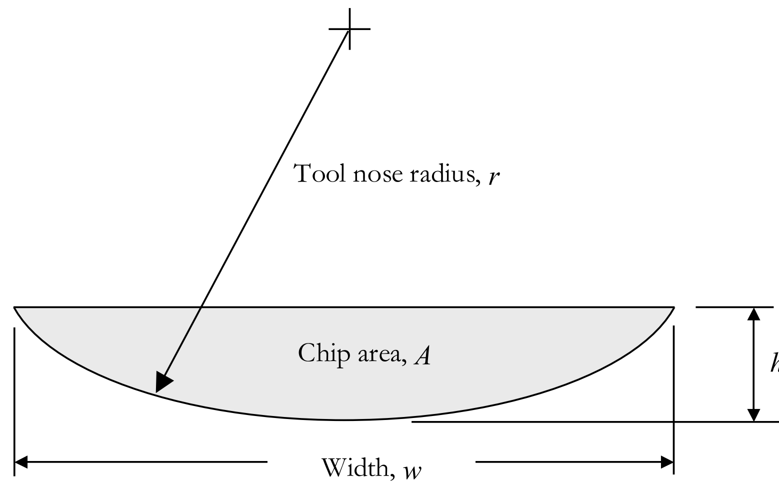

Figure 5.6: Geometry used to calculate the chip area, *A*.

A parabolic profile is used to approximate the round nosed diamond tool to make the chip area calculation much simpler. The approximate chip area, *A*, using the parabolic profile of tool nose is

$$A = \frac{4}{3} h \sqrt{2hr} \tag{5.14}$$

where *h* is the depth of cut and *r* is the tool nose radius. By substituting equation (5.3) in for the depth of cut, *h*, the chip area becomes:

$$A = \frac{L_1^3}{12R} \sqrt{\frac{r}{R}} \tag{5.15}$$

With a tool nose radius of 0.72 mm and a depth of cut of 1 μm, the parabolic profile assumption results in only a 0.1% error compared to the exact chip area.

CHAPTER 6

TEST RESULTS

This chapter presents the results of the silicon flycutting experiments. The results from the three different tool rake angles are discussed. In addition, the effect of crystal orientation on the critical chip thickness and thrust force is examined.

6.1 -45° RAKE ANGLE RESULTS

A distinct crystallographic dependence is found in the experimental data. As expected, a four-lobed pattern is observed in the force, critical chip thickness, and machining damage. A measured time capture of the thrust force for a 350° rotation of the workpiece is shown in Figure 6.1. This time trace is not a continuous time representation of the force data since the force is only captured for a small rotation of the flycutter.

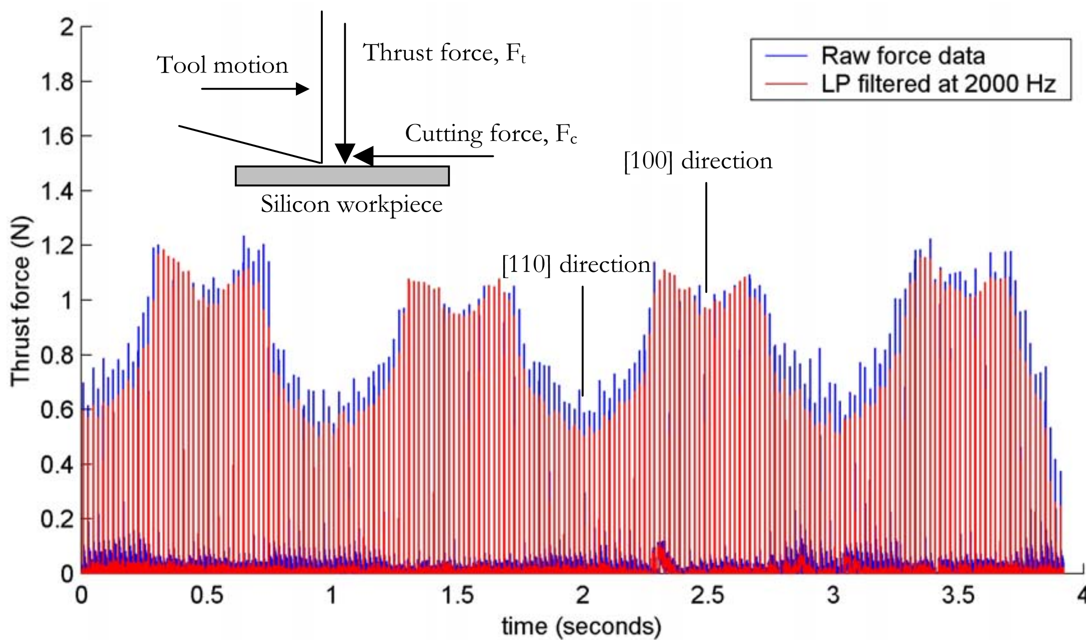

Figure 6.1: Measured thrust force time capture over 350° rotation of the workpiece spindle for a –45 degree rake diamond tool. The time capture is not a continuous time representation of the force data.

Figure 6.2 shows the polar plot of the normalized thrust force envelope taken from the raw data in Figure 6.1.

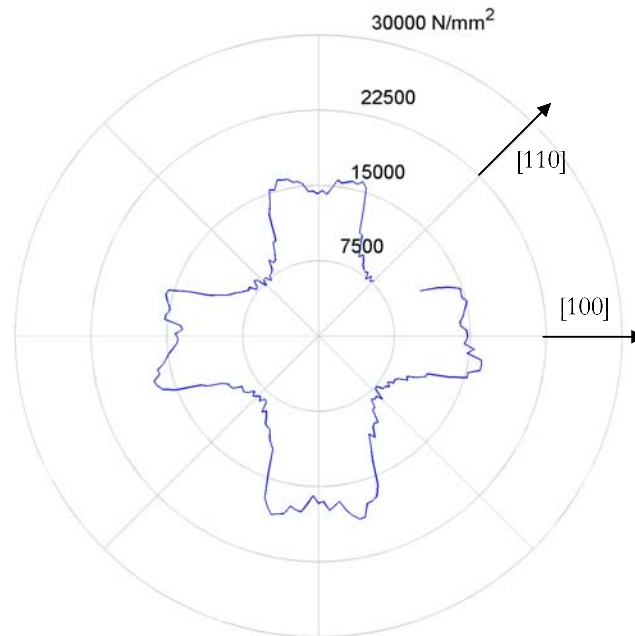

Figure 6.2: Normalized thrust force for a –45° rake tool around the (001) cubic face.

When comparing the pitting damage on the workpiece with Figure 6.2, the highly damaged regions on the workpiece correspond to the lower force regions on the polar plot. Figure 6.3 shows a schematic of the pitting damage observed on the workpiece.

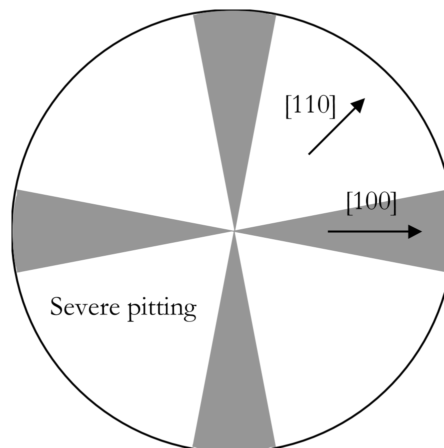

Figure 6.3: Schematic of the pitting damage on the (001) crystal face. The white regions correspond to high light scatter caused by severe pitting. In the darker regions, pitting is still present, but much less severe.

All other tests taken with the –45° rake tool support the findings shown in Figures 6.2 and 6.3. The force data follows the same four-lobed pattern for all other tests performed with the –45° rake tool. The force results of the other tests are found in Appendix B.

Figure 6.4 shows a Nomarski micrograph of a cut made in the [110] direction under 20x magnification. Notice the extreme pitting damage that occurs across the entire width of the cut.

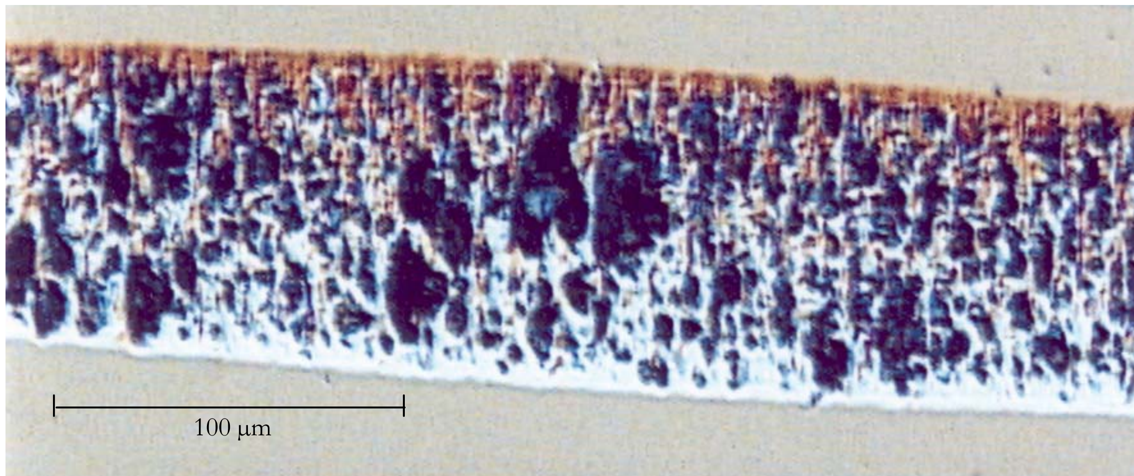

Figure 6.4: Nomarski micrograph of severe pitting damage in the [110] direction under 20x magnification. The depth of cut is 1.2 μm.

The orientation effect observed in the pitting damage makes sense from an energy standpoint. More energy is needed for ductile material removal than for brittle (fracture) material removal. Also, the <110> directions are the preferred slip directions for monocrystalline silicon. Therefore, less force is required to cause relative movement between the planes of atoms in this direction.

The variation in depth of cut is calculated by measuring the length of each cut around the (001) face. Figure 6.5 shows the depth of cut variation for the same test shown in Figure 6.2.

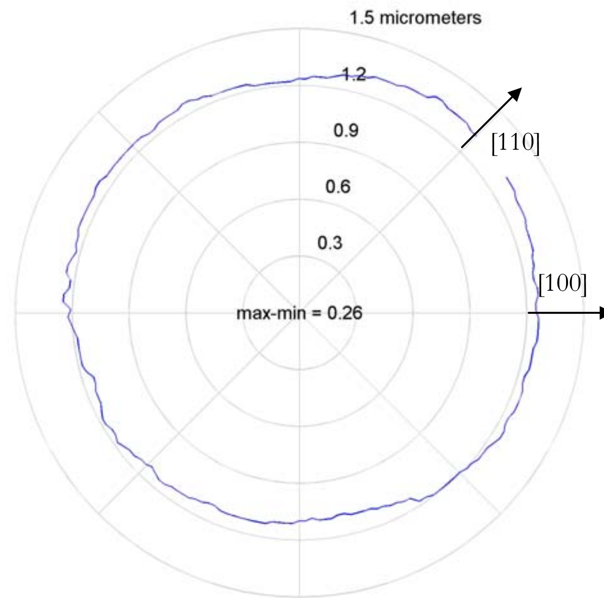

Figure 6.5: Variation in the depth of cut around the cubic crystal face.

The critical chip thickness is also found to exhibit the same four-lobed pattern as seen in the force trace. The dimensions of every cut around the (001) cubic face are measured and the critical chip thickness is calculated. Figure 6.6 shows the variation in critical chip thickness with orientation for a –45º rake tool.

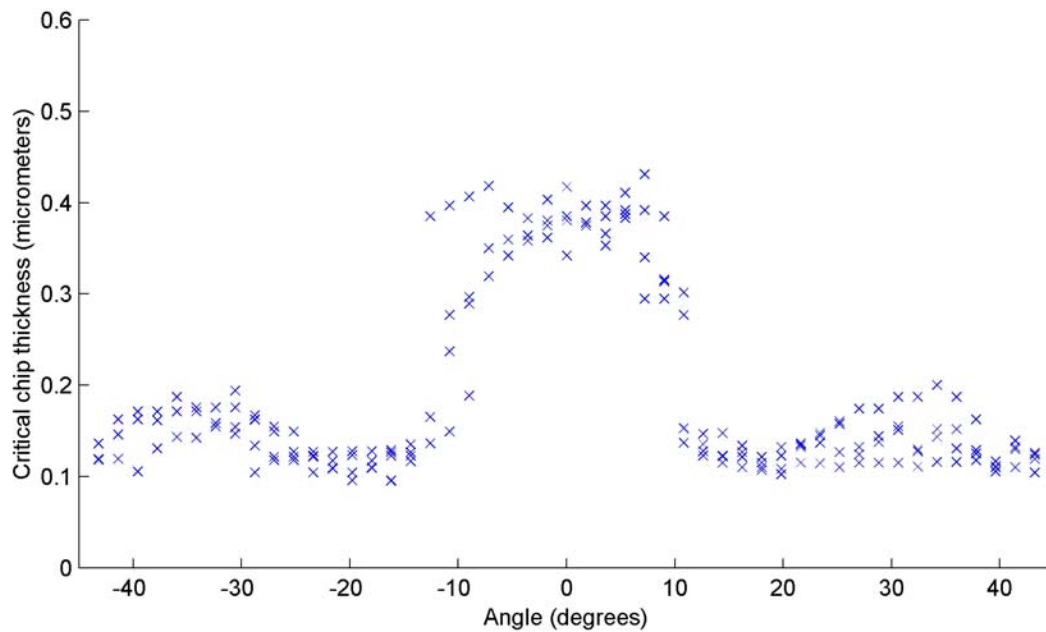

Figure 6.6: Variation of critical chip thickness with orientation. 0º corresponds to the [100] direction and ± 45º corresponds to the [110] directions.

When cutting in the [100] direction, the critical chip thickness is slightly less than 0.4 micrometers. In the [110] direction, the critical chip thickness is measured to be 0.1 micrometers. Thus, a four-fold increase is observed in the critical chip thickness when cutting in the [100] direction as compared to the [110] direction.

Figure 6.7 shows a Nomarski micrograph of two cuts: one in the [100] direction and one in the [110] direction. It is evident that the location in the cut where ductile material removal stops and brittle material removal starts to dominate is vastly different.

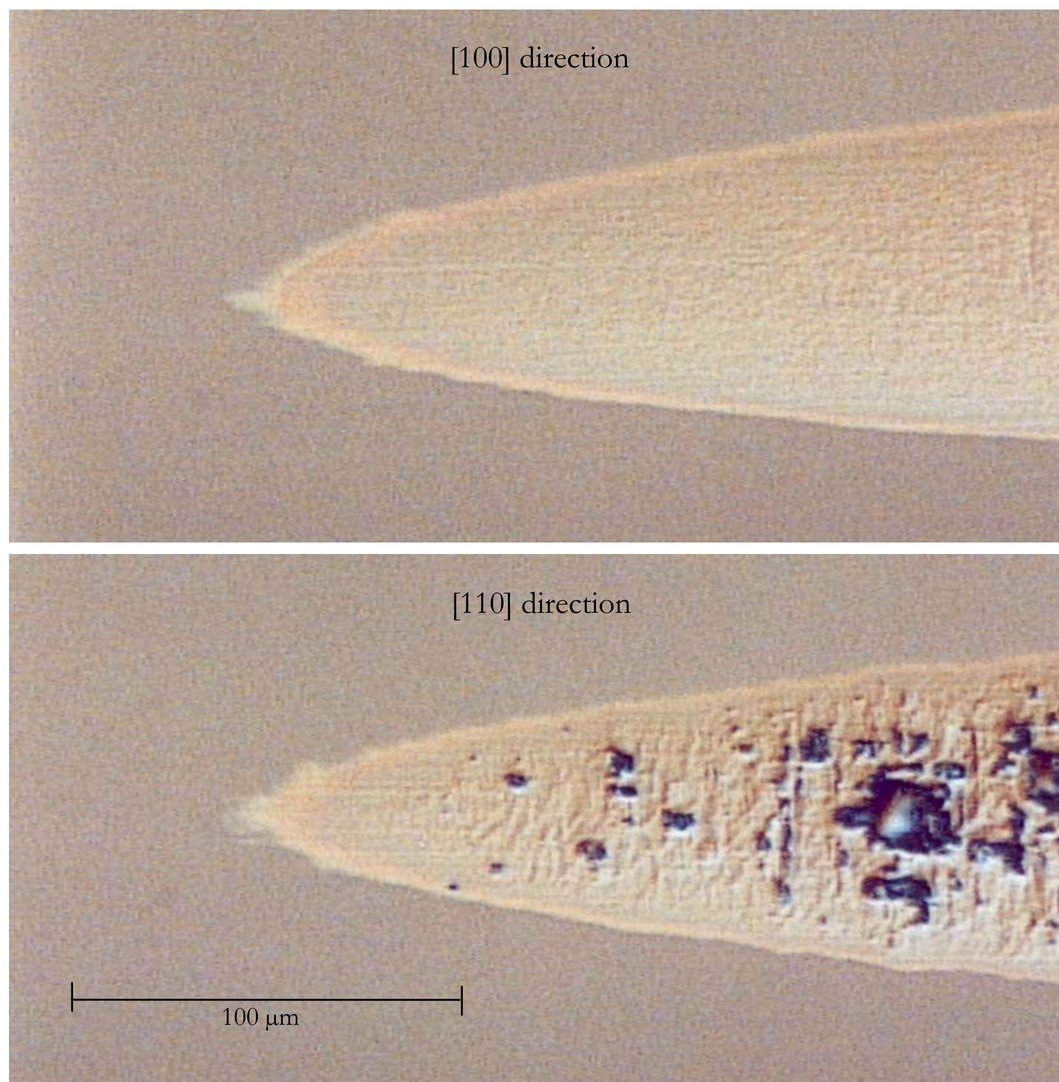

Figure 6.7: Nomarski micrograph of two cuts under 50x magnification. The top cut is in the [100] direction and the bottom is in the [110] direction.

6.2 0º AND –30º RAKE ANGLE RESULTS

Figure 6.8 shows an example of the normalized thrust force results for a 0º and –30ºrake tool.

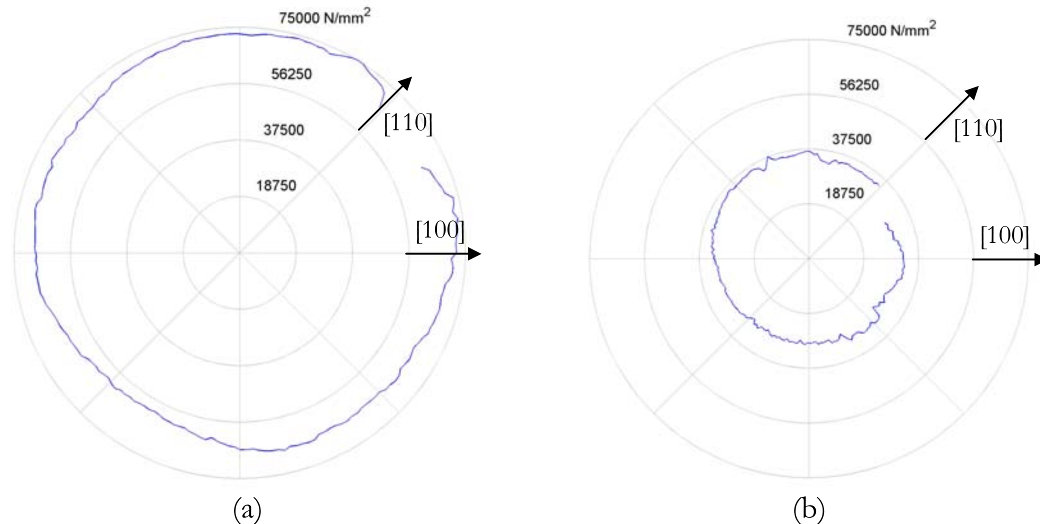

Figure 6.8: Normalized thrust force data for (a) 0º rake, 1.52 mm nose radius and (b) –30º rake, 1.60 mm nose radius.

Upon close examination of the diamond tools under an optical microscope, wear flats are found on the edge of both the 0º and –30º rake tools. A much larger wear flat is observed on the 0º rake tool than the –30º rake tool. This explains the much larger thrust forces observed with the 0º rake tool compared with the –30º rake tool.

The workpieces are inspected with an optical microscope and a scanning electron microscope. The machined grooves in both workpieces show the nose profile imparted into the machined grooves. The wear flats are due to previous use of the tools and not from the silicon flycutting experiments since the first cut made with each tool exhibits the same pattern as seen in Figure 6.9 for each cut.

The results from the flycutting tests for the 0º and –30º rake angles are inconclusive because of the worn tool edges. The wear marks are found to be present for all of the cuts made in the silicon workpiece with these tools. Therefore, the critical chip thickness is not characterized for these rake angles.

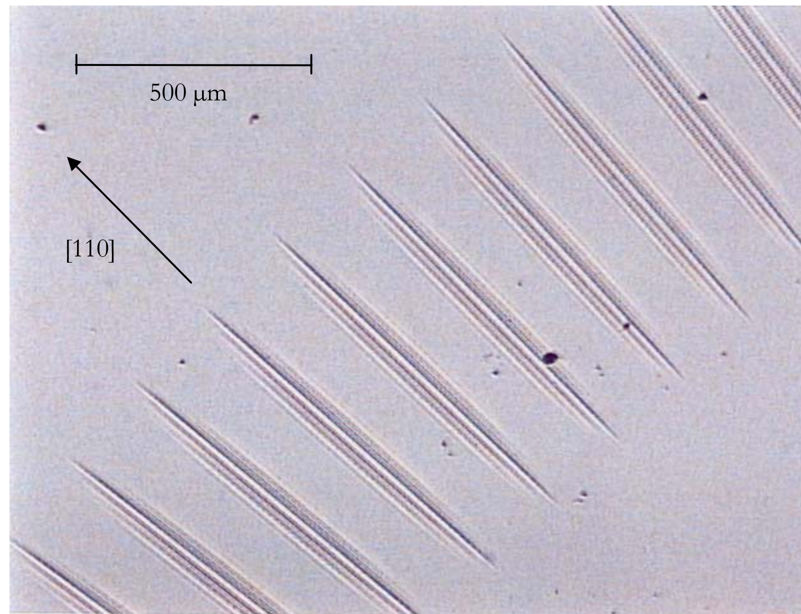

(a)

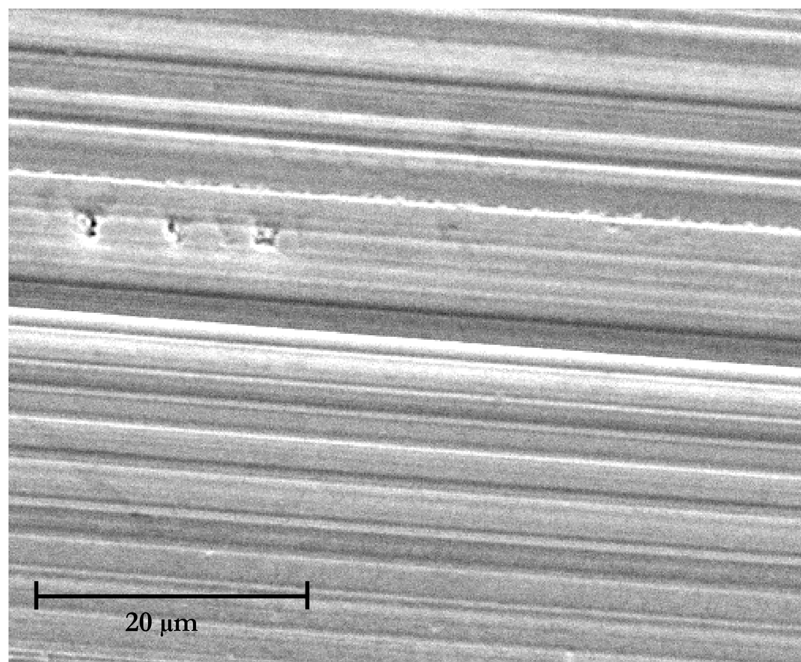

(b)

Figure 6.9: An example of cuts made in silicon with the worn 0º and –30º rake tools. (a) Bright-field microscopy micrograph of multiple cuts made in the [110] direction with a 0º rake tool. (b) An SEM micrograph of the bottom of a cut made with a 0º rake tool in the [110] direction.

CHAPTER 7

CONCLUSIONS AND FUTURE WORK

Silicon flycutting experiments are performed in order to characterize the critical chip thickness and machining force variation around the (001) silicon crystal face. The results from the –45º rake tool indicate that the critical chip thickness may vary by as much as 400% on the cubic face with the most favorable machining direction found to be the [100] direction.

If a silicon flat were to be machined by taking a facing cut on diamond turning lathe with the –45º rake tool, the chip thickness must be kept below 0.1 micrometers. However, if a diamond flycutting machine was used and the workpiece oriented such that cutting occurred in the [100] direction, then the chip thickness must be kept below 0.4 micrometers. A tremendous amount of savings could result because the feedrate could be increased four-fold.

The tests from the 0º and –30º rake tools are inconclusive because of badly worn tools. The wear flats found on these tools are from other experiments and not from the silicon flycutting tests. The worn tool nose profile is imparted in all of the cuts made with these tools; therefore, no useful data about the critical chip thickness and force variations can be extracted from these tests.

Future studies are planned to investigate the effect of tool rake angle and nose radius on the critical chip thickness variation. In addition, studies are planned to investigate the effect of crystal orientation on tool wear. Finally, the critical chip thickness results will be verified using facing cut and other flycutting geometries.

In conclusion, by taking advantage of the anisotropic machining properties of silicon, the machining parameters such as feedrate and depth of cut can be increased. This is sure to decrease production time, but the effects on tool wear are yet unknown.

APPENDIX A

TRANSFORMATION OF STIFFNESS AND COMPLIANCE MATRICES

An efficient matrix technique outlined in Auld [16] that uses 6x6 transformation matrices to transform stress and strain fields to other coordinate systems is presented. This technique is useful to transform the stiffness and compliance matrices for anisotropic crystals in order to calculate the variation of elastic properties on various crystal faces. Examples of the transformation of matrices are presented for the (001) and (011) crystal faces.

First, consider a stress field, σ_{ij}. In subscript notation, the transformation of the stress field to another coordinate system is given as

$$\sigma_{ij}' = a_{ik} a_{jl} \sigma_{kl} \qquad i, j, k, l = x, y, z \tag{A.1}$$

where σ_{ij}' is the stress field in transformed reference frame, σ_{kl} is the stress field in the original reference frame, and a_{ik}, a_{jl} are corresponding elements of the 3x3 direction cosine matrix between the transformed coordinate system and the reference coordinate system. The direction cosine matrix can be written as

$$[a] = \begin{bmatrix} a_{xx} & a_{xy} & a_{xz} \\ a_{yx} & a_{yy} & a_{yz} \\ a_{zx} & a_{zy} & a_{zz} \end{bmatrix} \tag{A.2}$$

Rewriting each stress term individually and examining the terms comprising of the transformed stress, one arrives at an abbreviated expression for the transformation

$$\sigma_H' = M_{HI} \sigma_H \qquad H, I = 1, 2, 3, 4, 5, 6 \tag{A.3}$$

where M_{HI} is known as the Bond stress transformation matrix. The Bond stress transformation matrix is given in terms of the direction cosine matrix components as

$$[M]=\begin{bmatrix} a_{xx}^2 & a_{xy}^2 & a_{xz}^2 & 2a_{xy}a_{xz} & 2a_{xz}a_{xx} & 2a_{xx}a_{xy} \\ a_{yx}^2 & a_{yy}^2 & a_{yz}^2 & 2a_{yy}a_{yz} & 2a_{yz}a_{yx} & 2a_{yx}a_{yy} \\ a_{zx}^2 & a_{zy}^2 & a_{zz}^2 & 2a_{zy}a_{zz} & 2a_{zz}a_{zx} & 2a_{zx}a_{zy} \\ a_{yx}a_{zx} & a_{yy}a_{zy} & a_{yz}a_{zz} & a_{yy}a_{zz}+a_{yz}a_{zy} & a_{yz}a_{zz}+a_{yz}a_{zx} & a_{yy}a_{zx}+a_{yx}a_{xy} \\ a_{zx}a_{xx} & a_{zy}a_{xy} & a_{zz}a_{xz} & a_{xy}a_{zz}+a_{xz}a_{zy} & a_{xz}a_{zx}+a_{xx}a_{zz} & a_{xx}a_{zy}+a_{xy}a_{zx} \\ a_{xx}a_{yx} & a_{xy}a_{yy} & a_{xz}a_{yz} & a_{xy}a_{yz}+a_{xz}a_{yy} & a_{xz}a_{yx}+a_{xx}a_{yz} & a_{xx}a_{yy}+a_{xy}a_{yx} \end{bmatrix} \quad \text{(A.4)}$$

Similarly, transformation of a strain field, ϵ_{ij}, can be written as

$$\varepsilon_{ij}' = a_{ik}\, a_{jl}\, \varepsilon_{ij}\,. \quad \text{(A.5)}$$

Following the same procedure as the transformed stress field, the resulting transformed strain field can be written in abbreviated notation as

$$\varepsilon_K' = N_{KJ}\,\varepsilon_J \qquad K, J = 1, 2, 3, 4, 5, 6 \quad \text{(A.6)}$$

where N_{KJ} is known as the Bond strain transformation matrix and is given as

$$[N]=\begin{bmatrix} a_{xx}^2 & a_{xy}^2 & a_{xz}^2 & a_{xy}a_{xz} & a_{xz}a_{xx} & a_{xx}a_{xy} \\ a_{yx}^2 & a_{yy}^2 & a_{yz}^2 & a_{yy}a_{yz} & a_{yz}a_{yx} & a_{yx}a_{yy} \\ a_{zx}^2 & a_{zy}^2 & a_{zz}^2 & a_{zy}a_{zz} & a_{zz}a_{zx} & a_{zx}a_{zy} \\ 2a_{yx}a_{zx} & 2a_{yy}a_{zy} & 2a_{yz}a_{zz} & a_{yy}a_{zz}+a_{yz}a_{zy} & a_{yz}a_{zz}+a_{yz}a_{zx} & a_{yy}a_{zx}+a_{yx}a_{xy} \\ 2a_{zx}a_{xx} & 2a_{zy}a_{xy} & 2a_{zz}a_{xz} & a_{xy}a_{zz}+a_{xz}a_{zy} & a_{xz}a_{zx}+a_{xx}a_{zz} & a_{xx}a_{zy}+a_{xy}a_{zx} \\ 2a_{xx}a_{yx} & 2a_{xy}a_{yy} & 2a_{xz}a_{yz} & a_{xy}a_{yz}+a_{xz}a_{yy} & a_{xz}a_{yx}+a_{xx}a_{yz} & a_{xx}a_{yy}+a_{xy}a_{yx} \end{bmatrix}. \quad \text{(A.7)}$$

Hooke's law can be written in matrix form as

$$[\sigma]=[c][\varepsilon] \quad \text{(A.8)}$$

where [c] is the material stiffness matrix. To transform the stress matrix a new coordinate system, the Bond stress transformation matrix can be applied as

$$[\sigma']=[M][c][\varepsilon] \quad \text{(A.9)}$$

where $[M]$ is the Bond stress transformation matrix and $[\sigma']$ is the transformed stress matrix. By taking the inverse of (A.6) and substituting into (A.9) results in

$$[\sigma'] = [M][c][S]^{-1}[\varepsilon'] \tag{A.10}$$

where the transformed stiffness matrix is

$$[c'] = [M][c][N]^{-1}. \tag{A.11}$$

The same can be done for the compliance matrix. Therefore, the transformed compliance matrix becomes

$$[s'] = [N][c][M]^{-1}. \tag{A.12}$$

Once the direction cosine (rotation) matrix is found, the Bond transformation matrices can be calculated from equations (A.4) and (A.7). Then, equations (A.11) and (A.12) can be used to calculate the transformed compliance and stiffness matrices.

A.1 Rotation around the (001) Crystal Face

For a cubic crystal, the stiffness matrix is given as

$$[c] = \begin{bmatrix} c_{11} & c_{12} & c_{12} & 0 & 0 & 0 \\ c_{12} & c_{11} & c_{12} & 0 & 0 & 0 \\ c_{12} & c_{12} & c_{11} & 0 & 0 & 0 \\ 0 & 0 & 0 & c_{44} & 0 & 0 \\ 0 & 0 & 0 & 0 & c_{44} & 0 \\ 0 & 0 & 0 & 0 & 0 & c_{44} \end{bmatrix}. \tag{A.13}$$

For calculating the stiffness or compliance matrix around the (001) face, the rotation matrix must first be calculated. For a clockwise rotation of angle θ about the [001] axis, the rotation matrix is given as

$$[a] = \begin{bmatrix} cos\theta & sin\theta & 0 \\ -sin\theta & cos\theta & 0 \\ 0 & 0 & 1 \end{bmatrix}. \tag{A.14}$$

Therefore, substituting the appropriate terms into the equations for $[M]$ and $[N]$ and performing the calculation in equation (A.11), the transformed stiffness matrix becomes

$$[c'] = \begin{bmatrix} c_{11}' & c_{12}' & c_{13}' & 0 & 0 & c_{16}' \\ c_{12}' & c_{11}' & c_{13}' & 0 & 0 & -c_{16}' \\ c_{13}' & c_{13}' & c_{33}' & 0 & 0 & 0 \\ 0 & 0 & 0 & c_{44}' & 0 & 0 \\ 0 & 0 & 0 & 0 & c_{44}' & 0 \\ c_{16}' & -c_{16}' & 0 & 0 & 0 & c_{66}' \end{bmatrix} \tag{A.15}$$

where

$$c_{11}' = c_{11} - \left(\frac{c_{11} - c_{12}}{2} - c_{44} \right) sin^2 2\theta$$
$$c_{12}' = c_{12} + \left(\frac{c_{11} - c_{12}}{2} - c_{44} \right) sin^2 2\theta$$
$$c_{13}' = c_{12}$$
$$c_{16}' = -\left(\frac{c_{11} - c_{12}}{2} - c_{44} \right) sin 2\theta \, cos 2\theta$$
$$c_{33}' = c_{11}$$
$$c_{44}' = c_{44}$$
$$c_{66}' = c_{44} + \left(\frac{c_{11} - c_{12}}{2} - c_{44} \right) sin^2 2\theta$$

The same procedure can be applied for the calculation of the transformed compliance matrix. Once the transformed compliance matrix is calculated, the variation of the elastic modulus around the (001) face is given as

$$E_{001} = \frac{1}{s_{11}'} \tag{A.16}$$

where s_{11}' is the transformed compliance component around the (001) face.

A.2 ROTATION AROUND THE (011) CRYSTAL FACE

For a rotation around the (011) crystal face, the transformed compliance matrix must be calculated in two separate steps. First, a 45° counter-clockwise rotation around the [010] cubic axis is performed. The rotation matrix for this first rotation is

$$[a]_1 = \begin{bmatrix} \frac{\sqrt{2}}{2} & 0 & \frac{\sqrt{2}}{2} \\ 0 & 1 & 0 \\ -\frac{\sqrt{2}}{2} & 0 & \frac{\sqrt{2}}{2} \end{bmatrix}. \tag{A.17}$$

By applying equation (A.11), the transformed stiffness matrix becomes

$$[c'] = \begin{bmatrix} c_{11}' & c_{12}' & c_{13}' & 0 & 0 & 0 \\ c_{12}' & c_{22}' & c_{12}' & 0 & 0 & 0 \\ c_{13}' & c_{12}' & c_{11}' & 0 & 0 & 0 \\ 0 & 0 & 0 & c_{44}' & 0 & 0 \\ 0 & 0 & 0 & 0 & c_{55}' & 0 \\ 0 & 0 & 0 & 0 & 0 & c_{44}' \end{bmatrix} \tag{A.18}$$

where

$$\begin{aligned} c_{11}' &= \frac{1}{2}(c_{11} + c_{12} + 2c_{44}) \\ c_{12}' &= c_{12} \\ c_{13}' &= \frac{1}{2}(c_{11} + c_{12} - 2c_{44}) \\ c_{22}' &= c_{11} \\ c_{44}' &= c_{44} \\ c_{55}' &= \frac{1}{2}(c_{11} - c_{12}). \end{aligned}$$

The next rotation is a clockwise rotation of angle θ about the transformed [001] axis. The rotation matrix for the second transformation is given as

$$[a]_2 = \begin{bmatrix} cos\theta & sin\theta & 0 \\ -sin\theta & cos\theta & 0 \\ 0 & 0 & 1 \end{bmatrix}. \quad \text{(A.19)}$$

Therefore, the transformed stiffness matrix is

$$[c''] = [M]_2 [c'][N]_2^{-1} \quad \text{(A.20)}$$

where $[M]_2$ and $[N]_2$ are the Bond stress and strain transformation matrices, respectively, for the second rotation matrix given in equation (A.19). The results of equation (A.20) are quite cumbersome; therefore, they are not shown.

The methods outlined in this appendix allow relatively simple calculation of the elastic properties of a crystal with a given material stiffness or compliance matrix. Although the examples were shown using a cubic crystal stiffness matrix, this method is applicable to more complex crystal stiffness or compliance matrices.

APPENDIX B

-45° RAKE ANGLE FORCE RESULTS

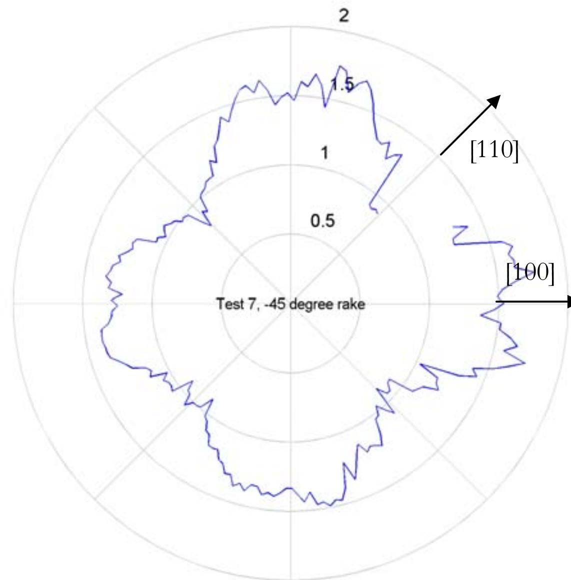

Figure A.1: Thrust force around cubic crystal face for a nominal depth of cut of 1.0 μm: Test 7, Workpiece 3.

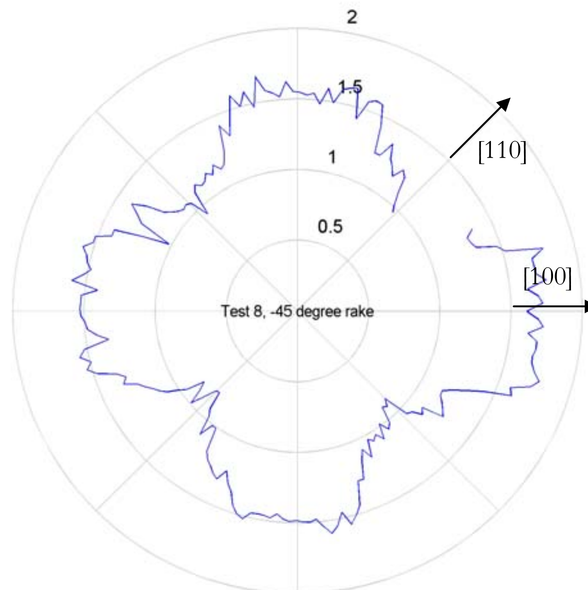

Figure A.2: Thrust force around cubic crystal face for a nominal depth of cut of 0.75 μm: Test 8, Workpiece 3.

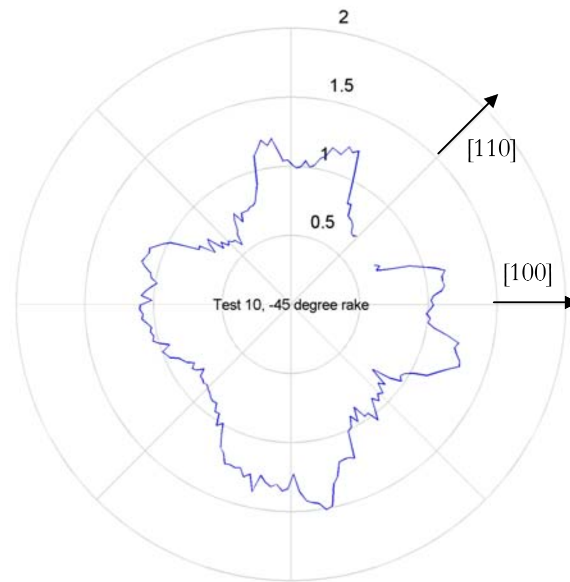

Figure A.3: Thrust force around cubic crystal face for a nominal depth of cut of 0.3 μm: Test 10, Workpiece 4.

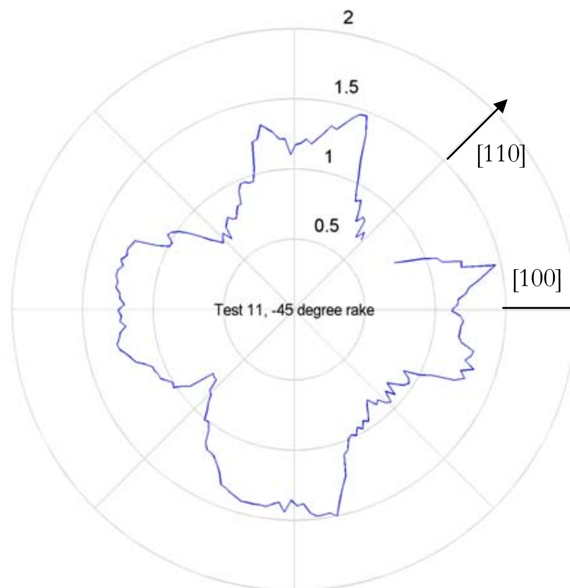

Figure A.4: Thrust force around cubic crystal face for a nominal depth of cut of 0.4 μm: Test 11, Workpiece 4.

REFERENCES

[1] Taniguchi, N., "Current Status in, and Future Trends of, Ultraprecision Machining and Ultrafine Materials Processing." *Annals of the CIRP*, v 32, n 2, 1983, pp. 573-582.

[2] Moore, W., *Foundations of Mechanical Accuracy*. Moore Special Tool Company, 1970.

[3] Ikawa, N., Donaldson, R., et. al., "Ultraprecision Metal Cutting – The Past, Present and Future." *Annals of the CIRP*, v 40, n 2, 1991, pp.587-594.

[4] Krauskopf, B., "Diamond Turning: Reflecting the Demands for Precision." *Manufacturing Engineering*, v 92, 1984, pp. 90-100.

[5] Bryan, J., "Design and Construction of an Ultraprecision 84 inch Diamond Turning Machine." *Precision Engineering,* v 1, n 1, 1979, pp. 13-17.

[6] Donaldson, R., and Patterson, S., "Design and Construction of a Large, Vertical Axis Diamond Turning Machine." *LLNL UCRL-89738*, 1983.

[7] Saito, T., "Machining of Optics: An Introduction." *Applied Optics*, v 14, n 8, 1975, pp. 1773-1776.

[8] Miller, J., *Principles of Infrared Technology: A Practical Guide to the State of the Art*. New York: Van Nostrand Reinhold, 1994.

[9] Ahmad, A., *Handbook of Optomechanical Engineering*. Florida: CRC Press, 1997.

[10] McKeown, P., "From Micro- to Nano-machining – Towards the Nanometre Era." *Sensor Review*, v 16, n 2, 1996, pp. 4-10.

[11] Sreejith, P., Udupa, Y., Noor, Y., and Ngoi, B.,. "Recent Advances in Machining Silicon Wafers for Semiconductor Applications." *International Journal of Advanced Manufacturing Technology*, v 17, 2001, pp. 157-162.

[12] Paul, E., Evans, C., Mangamelli, A., McGlauflin, M., and Polvani, R. "Chemical aspects of tool wear in diamond turning." *Precision Engineering,* v 18, n 1, 1996, pp. 4-19.

[13] Shimura, F., *Semiconductor Silicon Crystal Technology*. San Diego: Academic Press, 1989.

[14] Shaw, M.C., "Precision Finishing." *Annals of the CIRP,* v 44, n 1, 1995, pp. 343-348.

[15] Kim, George. "Technical Details of Silicon Machining Behavior from a Diamond Toolmaker's Perspective." *Proceedings of ASPE Spring Topical Meeting on Silicon Machining*, 1998.

[16] Auld, B., *Acoustic Fields and Waves in Solids.* v 1, 2nd ed., Florida: Robert E. Krieger Publishing Company, 1990.

[17] Kittel, C., *Introduction to Solid State Physics.* 3rd ed., New York: John Wiley and Sons, Inc., 1956.

[18] Nye, J., *Physical Properties of Crystals.* Oxford: Clarendon Press, 1957.

[19] Lekhnitski, S., *Theory of Elasticity of an Anisotropic Body.* San Francisco: Holden-Day, Inc., 1963.

[20] Collins, J., Giardini, W., Leistner, A., and Kenny, M., "The Influence of Young's Modulus on the Roundness in Silicon Sphere Fabrication." *Proceedings of the 1996 Conference on Precision Electromagnetic Measurements*,
Jun 17-20 1996, pp. 466-467.

[21] Callister, W., *Materials Science and Engineering: An Introduction.* 4th ed., New York: John Wiley and Sons, Inc., 1997.

[22] Wonsiewicz, B., and Chin, G., "Chapter 12: A Theory of Knoop Hardness Anisotropy." *Science of Hardness Testing and its Applications.* Ohio: American Society of Metals, 1973.

[23] Brookes, C., and Burnand, R., "Chapter 15: Hardness Anisotropy in Crystalline Solids." *Science of Hardness Testing and its Applications.* Ohio: American Society of Metals, 1973.

[24] Chen, C., and Leipold, M. "Fracture Toughness of Silicon." *American Ceramic Society Bulletin.* v 59, n 4, 1980, pp. 469-472.

[25] Lawn, B., and Wilshaw, R. "Indentation Fracture: Principles and Applications." *Journal of Materials Science*, v 10, 1975, pp. 1049-1081.

[26] Kendall, K., "Complexities of Compression Failure." *Proceedings of the Royal Society of London, Series A*, v 361, 1978, pp. 245-263.

[27] Hawman, M., Cohen, P., Conway, J., and Pangborn, R., "Effect of Grinding on the Flexural Strength of Sialon Ceramic." *Journal of Materials Science*, v 20, n 2, pp. 482-490.

[28] Malkin, S., and Hwang, T., "Grinding Mechanisms for Ceramics." *Annals of the CIRP*, v 45, n 2, 1996, pp. 569-580.

[29] Lawn, B., and Swain, M., "Microfracture Beneath Point Indentations in Brittle Solids." *Journal of Material Science*, v 10, 1975, pp.113-122.

[30] Swain, M., "Microfracture About Scratches in Brittle Solids." *Proceedings of the Royal Society of London, Series A*, v 366, 1979, pp. 575-597.

[31] Lawn, B., and Evans, A.G., "A Model for Crack Initiation in Elastic/Plastic Indentation Fields." *Journal of Materials Science*, v 12, 1977, pp. 2195-2199.

[32] Lawn, B., Jensen, T., and Arora, A., "Brittleness as an Indentation Size Effect." *Journal of Material Science* , v 11, 1976, pp. 573-575.

[33] Lawn, B., "Partial Cone Crack Formation in a Brittle Material Loaded with a Sliding Spherical Indenter." *Proceedings of the Royal Society of London, Series A*, v 299, 1967, pp. 307-316.

[34] Syn, C., Taylor, J., Donaldson, R., and Shimada, S., "Ductile-brittle Transition of Cutting Behavior in Diamond Turning of Single Crystal Silicon." *LLNL UCRL-98100*, 1988.

[35] Bifano, T., Dow, T., and Scattergood, R., "Ductile-Regime Grinding of Brittle Materials: Experimental Results and Development of a Model." *Proceedings of the SPIE: Advances in Fabrication and Metrology for Optics and Large Optics*, v 966, 1988, pp. 108-115.

[36] Blake, P., and Scattergood, R., "Ductile-Regime Machining of Germanium and Silicon." *Journal of the American Ceramic Society*, v 73, n 4, 1990, pp. 949-957.

[37] Morris, J., Callahan, D., Kulik, J., Patten, J., and Scattergood, R., "Origins of the Ductile-Regime in Single-Point Diamond Turning of Semiconductors." *Journal of the American Ceramic Society*, v 78, n 8, 1995, pp. 2015-2020.

[38] Brinksmeier, E., Preub, W., Riemer, O., and Malz, R., "Ductile to Brittle Transition Investigated by Plunge-cut Experiments in Monocrystalline Silicon." *Proceedings of the ASPE 1998 Spring Topical Meeting*, v 17, 1998, pp. 55-58.

[39] Blaedel, K., Taylor, J., and Evans, C., "Ductile-Regime Grinding of Brittle Materials." *Machining of Ceramics and Composites*. Ed. Jahanmuir, S., Ramulu, M., and Koshy, P. New York: Marcel Dekker, Inc., 1999, pp. 139-176.

[40] Blackley, W., and Scattergood, R., "Crystal Orientation Dependence of Machining Damage – A Stress Model." *Journal of the American Ceramic Society*, v 73, n 10, 1990, pp. 3113-3115.

[41] Shibata, T., Fujii, S., Makino, E., and Ikeda, M., "Ductile-Regime Turning Mechanism of Single-Crystal Silicon." *Precision Engineering*, v 18, n 2/3, 1996, pp. 129-137.

[42] Hung, N., and Fu, Y., "Effect of Crystalline Orientation in the Ductile-Regime Machining of Silicon." *International Journal of Advanced Manufacturing Technology*, v 16, 2000, pp. 871-876.

[43] Lee, W., To, S., and Cheung, C., "Effect of Crystallographic Orientation in Diamond Turning of Copper Single Crystals." *Scripta Materialia*, v 42, 2000, pp. 937-945.

[44] ANSI/ASME B5.54-1992, *Methods for Performance Evaluation of Computer Numerically Controlled Machining Centers*. New York: ASME, 1992.